Economic Geology, v. XXX, no. XX, pp. X–X

Establishing Mineral Chemical Vectors Toward Metamorphosed Volcanic-Hosted Massive Sulfide Deposits: New Insights from Chlorite, White Mica, and Garnet

Cendi D.P. Dana,[1,†] Steven P. Hollis,[1] Paul G. Spry,[2] Conal J. Rodgers,[1,3] Megan James,[4] Darryl Podmore,[4] and Riquan Azri[4]

[1]*School of GeoSciences, Grant Institute, The University of Edinburgh, Edinburgh EH9 3FE, United Kingdom*

[2]*Department of the Earth, Atmosphere and Climate, Iowa State University, Ames, Iowa 50011-1037, USA*

[3]*SLR Consulting, The Tun, 4 Jackson's Entry, Edinburgh EH8 8PJ, United Kingdom*

[4]*Black Raven Mining, PO Box 902, West Perth, Western Australia 6872, Australia*

Abstract

This study assesses the potential of chlorite, white mica, and garnet chemistry, coupled with hyperspectral data, as vectoring tools in metamorphosed volcanic-hosted massive sulfide (VHMS) deposits. Samples were collected from the King Zn deposit of the Eastern Goldfields superterrane, Yilgarn craton, which was metamorphosed to the amphibolite facies. In situ chlorite-white mica chemical trends match the shifting positions of the 2,200W and 2,250W absorption features obtained by short-wave infrared (SWIR) spectroscopy. These include a shift from muscovite to Na muscovite in the felsic footwall approaching mineralization, to phengite in the hanging wall, and mostly mixed Fe-Mg chlorite compositions with shifts to Mg-rich chlorite in the Mg-metasomatized felsic footwall. Fluorine (up to 2,500 ppm) and Mn (up to 1.1 wt %) contents of chlorite increase systematically through the footwall of the deposit toward the massive sulfide but drop sharply in the hanging wall—a trend mirrored in F contents in white mica (up to 2,500 ppm) and Mn in garnet (up to 17 wt %). These variations are attributed to premetamorphic footwall metasomatism and can trace hydrothermal up-flow zones in metamorphosed VHMS systems. Thermal infrared (TIR) signatures (11,100W and 11,300DW) correlate negatively with almandine and positively with spessartine contents in garnet, while rare earth element (REE) profiles of garnet further aid in the assessment of VHMS prospectivity. Positive Eu anomalies and downward-dipping heavy rare earth element (HREE) profiles in garnet enriched in the almandine end member distinguish mineralization-related garnet from those of barren metamorphic or igneous origins. Several elements, including Sr-Ba-Rb contents in white mica, Al in chlorite, and Ca-Mn with positive Eu anomalies in garnet, also differentiate footwall from least altered hanging-wall units. This study highlights the effectiveness of integrating chlorite, white mica, and garnet chemistry with hyperspectral data for regional VHMS exploration in high-grade metamorphic terranes.

Introduction

In recent years, extensive research has been conducted to explore the application and potential of mineral chemistry as a vectoring tool in metamorphosed massive sulfide deposits, including volcanic-hosted massive sulfide (VHMS) deposits. Several minerals, such as chlorite (e.g., Soltani Dehnavi et al., 2019; Gisbert et al., 2022), white mica (e.g., Soltani Dehnavi et al., 2018; Gisbert et al., 2022), amphibole (e.g., Drummond et al., 2020; Spry et al., 2024), gahnite (e.g., Heimann et al., 2005; O'Brien et al., 2015), magnetite (e.g., Makvandi et al., 2016a; Spry et al., 2024), and carbonate (e.g., Gisbert et al., 2022), have been demonstrated to provide discrimination of alteration types and/or robust halos to mineralization. Additionally, garnet has been demonstrated to be a reliable vectoring tool in some metamorphosed sediment-hosted deposits (e.g., Nesbitt, 1982; Spry et al., 2007; Heimann et al., 2011; Pollock et al., 2018; Tott et al., 2019; Lisboa et al., 2023), though only limited data have been reported from VHMS systems (e.g., Yeats and Groves, 1998; Mercier-Langevin et al., 2007; Hassan, 2017). These studies support the concept that garnet proximal to massive sulfide mineralization has higher Mn contents than distal or regional metamorphic garnet, which is generally enriched in the almandine component.

In addition to mineral chemistry, numerous studies have demonstrated the effectiveness of hyperspectral techniques to aid in the exploration of VHMS deposits (e.g., van Ruitenbeek et al., 2012; Duuring et al., 2016; Hassan, 2017; Hollis et al., 2019a, 2021; Dana et al., 2025). Systematic shifts in the composition of white mica and chlorite using short-wave infrared (SWIR) absorption signatures at about 2,200 and 2,250 nm, respectively, can provide useful halos to mineralization and also discriminate between footwall and hanging-wall stratigraphy (e.g., Hollis et al., 2021; Dana et al., 2025). Shifts from longer to shorter wavelengths in white mica (>2,200 nm to 2,190–2,200 nm) can reflect changes from Al-poor to Al-rich mica, which can also align with a shift from K-rich to Na-rich compositions (Cloutier et al., 2021; Salama et al., 2025). In both the King and Nimbus VHMS deposits of Western Australia, systematic shifts have been noted from muscovite to Na-rich muscovite approaching VHMS mineralization in footwall rocks and more phengitic (i.e., longer wavelengths) in the stratigraphic hanging wall (Hollis et al., 2021; Dana et al., 2025). Chlorite spectral signatures have also been shown to vary according to protolith composition, alteration style, and intensity, with trends of Mg enrichment toward mineralization observed in some deposits (e.g., King deposit, Dana et

[†]Corresponding author: email, c.d.p.dana@sms.ed.ac.uk

ISSN 0361-0128; doi:10.5382/econgeo.5206; 24 p.

Submitted: April 3, 2025 / Accepted: August 18, 2025

Digital appendices are available in the online Supplements section.

al., 2025), and the opposite trend of Fe enrichment in others (e.g., Golden Grove, Sharpe, 1999; Teutonic Bore, Thompson et al., 2009). Additionally, garnet chemistry can be obtained through thermal infrared (TIR) absorption features at 11.3 µm (Laukamp et al., 2021).

Given that only 11% of global VHMS discoveries occur in host sequences metamorphosed to the amphibolite facies and 0.5% in granulite facies rocks (Dusel-Bacon, 2012), robust tools for exploration are critical to increasing discovery rates in these terranes. These tools include further criteria for recognizing VHMS-proximal hydrothermally altered footwall rocks, their effective discrimination from distal footwall alteration, and weakly/unaltered hanging-wall rocks. Coupled hyperspectral and in situ mineral chemistry can help in identifying both mineralogical variations due to protolith composition and those caused by hydrothermal alteration (Large et al., 2001; Gibson et al., 2007). This approach can therefore quickly aid exploration companies in locating potential orebodies and prioritizing new exploration targets.

Here we present systematic major and trace element mineral chemical data from the King Zn deposit located in the Erayinia region of the Eastern Goldfields superterrane, Yilgarn craton. The King deposit represents an amphibolite facies-metamorphosed bimodal VHMS system, where the footwall stratigraphy varies in both protolith composition and alteration style, making it an ideal setting in which to evaluate the influence of lithology and alteration on mineral chemical trends. This deposit has a total resource (non-JORC compliant; JORC = Joint Ore Reserves Committee) of 2.15 million metric tonnes at 3.47% Zn, 0.3% Pb, 15 g/t Ag, and 0.2 g/t Au. Major and trace element data for chlorite, white mica, and garnet from representative drill holes covering the footwall; massive ore lens; and hanging-wall sequences were chemically and spectrally evaluated. Our new mineral chemical halos can be applied as a robust vectoring tool along a 45-km strike length of prospective greenstone stratigraphy in the Erayinia region, and also globally in terranes metamorphosed to the amphibolite facies.

Geologic Background

VHMS mineralization in the Yilgarn craton

The Yilgarn craton is subdivided into seven main terranes based on lithological associations, geochemistry, and ages of volcanism (Cassidy et al., 2006). These include the Southwest, Youanmi, Narryer, Kalgoorlie, Kurnalpi, Burtville, and Yamarna terranes, where the latter four together form the Eastern Goldfields superterrane. The geologic evolution of each terrane has been well described in numerous studies (e.g., Czarnota et al., 2010; Mole et al., 2014; Goscombe et al., 2019). In the Yilgarn craton, occurrences of VHMS mineralization are restricted to two main zones of thinned, juvenile crust (e.g., Huston et al., 2014; Mole et al., 2014; Osei et al., 2021), which are interpreted as Archean paleorift zones: (1) the Cue zone of the northern Youanmi terrane and (2) northerly-trending Kalgoorlie-Kurnalpi rift zone in the Eastern Goldfields superterrane (Huston et al., 2014; Hollis et al., 2015, 2017; Witt et al., 2018).

The timing of VHMS mineralization-forming events in the Youanmi terrane can be further divided into four main periods: (1) >2930 Ma, associated with early bimodal mafic greenstone belts (e.g., Golden Grove camp, Mount Gibson, and Weld Range; Yeats and Groves, 1998; Sharpe and Gemmell, 2002; Guilliamse, 2014); (2) ca. 2815 to 2800 Ma, associated with major plume and large igneous complex emplacement at shallow crust, with mineralization hosted in the Kantie Murdana Volcanics Member and Yaloginda Formation of the broader Norie Group (e.g., Austin-Quinns, Just Desserts, and Yuinmery deposits; Ivanic et al., 2010; Hassan, 2014; Duuring et al., 2016); (3) ca. 2760 to 2745 Ma, associated with rift-related magmatism in the Greensleeves Formation of the broader Polelle Group (e.g., Hollandaire, Jillewarra, Mt. Mulchay, and Dalgaranga; Hayman et al., 2015); and (4) ca. 2725 Ma, within the Gum Creek greenstone belt of the northeast Youanmi terrane (e.g., Altair, Bevan, and The Cup; Ivanic et al., 2010; Hollis et al., 2017). In contrast, most VHMS mineralization in the Eastern Goldfields superterrane is closely associated with bimodal volcanic complexes formed ca. 2720 to 2680 Ma (e.g., Anaconda, Nimbus, Teutonic Bore camp; Belford, 2010; Hollis et al., 2015, 2017; Barrote et al., 2020). Across the Yilgarn craton, VHMS mineralization also has a close temporal and spatial relationship with high field strength element (HFSE)–enriched granitoids and felsic volcanic rocks (Hollis et al., 2017). In the Eastern Goldfields superterrane, these can be found mostly in the Gindalbie domain of the Kurnalpi terrane (i.e., near the Teutonic Bore camp).

Local geology

The King Zn deposit occurs in the Erayinia region at the southernmost portion of the Kurnalpi terrane. The geology of the Erayinia region is described in the 1:100,000 Geological Survey of Western Australia regional report of Jones (2007), which is summarized here. The King Zn deposit is located in the far south Edjudina domain east of the Claypan fault (Fig. 1B), which is dominated by mafic-felsic volcanic complexes and laterally extensive belts of intermediate schist (Swager, 1995, 1997). This sequence is typically capped by banded iron formations (BIF), chert, and other metasedimentary rocks that are crosscut by later dolerite sills (Swager, 1995, 1997; Jones, 2007). The greenstone stratigraphy is metamorphosed to the amphibolite facies surrounding large granitic intrusions and to the greenschist facies in the central parts of greenstone belts (Jones, 2007). Detailed mineralogical and geochemical descriptions of the host stratigraphy are presented in several previous studies (e.g., Hollis et al., 2019b; Kelly et al., 2024; Dana et al., 2025).

The King Zn deposit is an overturned metamorphosed bimodal-felsic VHMS system metamorphosed to the amphibolite facies (e.g., Hollis et al., 2019b; Kelly et al., 2024) during M_2 regional contact metamorphism ca. 2685 to 2665 Ma (Goscombe et al., 2019). The footwall sequence can be divided into two main groups composed of mafic and felsic volcanic-derived lithologies. The deeper mafic footwall consists of mafic-derived metasedimentary rocks (biotite-muscovite schist) and tholeiitic metabasalt (garnet amphibolite). The overlying stratigraphic felsic footwall consists of calc-alkaline dacitic to rhyolitic metavolcanic/volcaniclastic rocks that can be divided into three mappable units: upper chlorite-muscovite-quartz schist, Mg-metasomatized muscovite-chlorite schist, and lower chlorite-muscovite-quartz schist (App. Fig. A1). Mas-

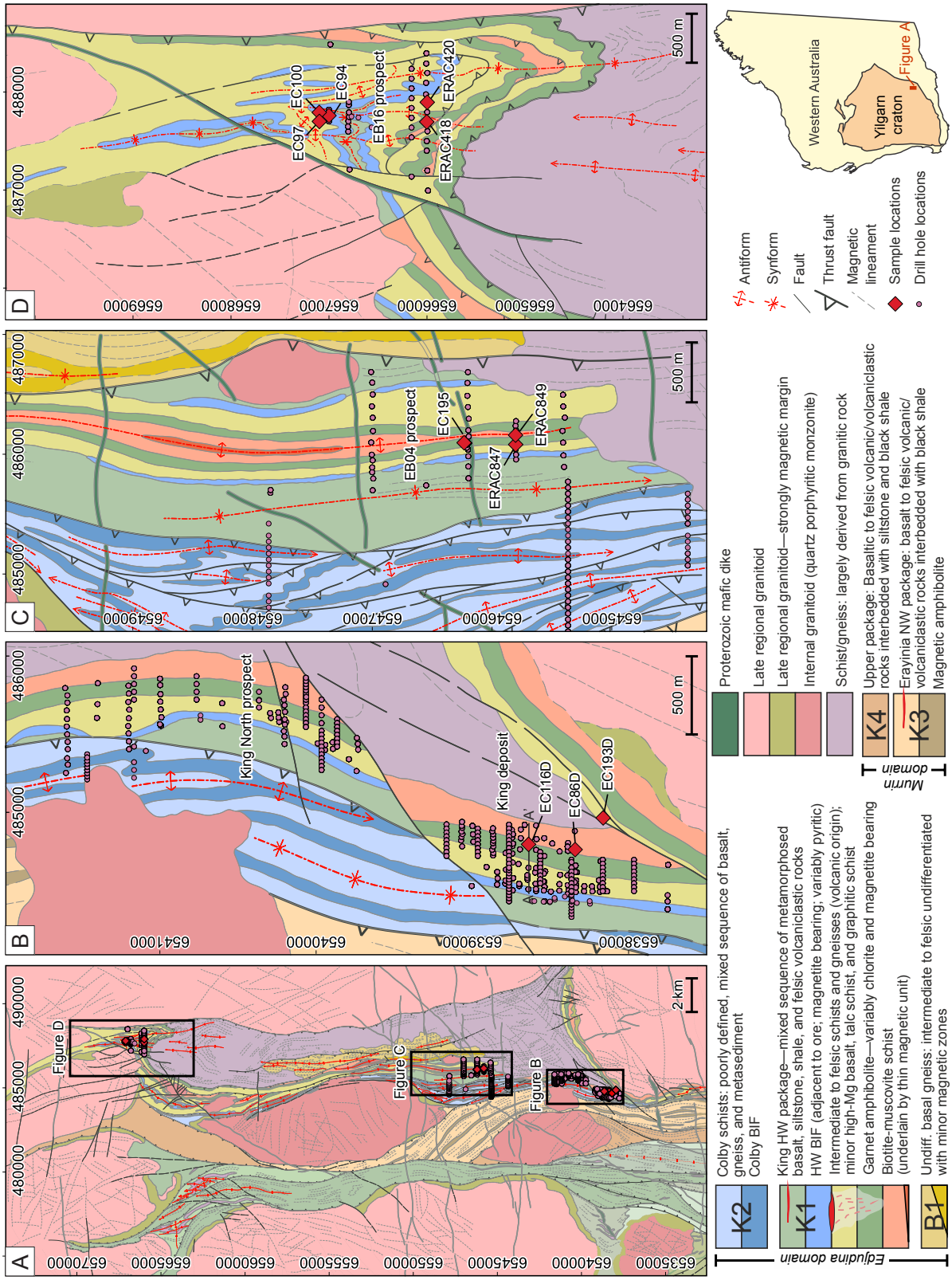

Fig. 1. (A) Regional geologic map of the King deposit and surrounding regional prospects (i.e., King North, EB04, and EB16). Detailed maps of each location are enlarged in B-D. Abbreviations: BIF = banded iron formation, HW = hanging wall, Undiff. = undifferentiated.

sive sulfide mineralization occurs at the contact between the upper chlorite-muscovite-quartz schist and an overlying hanging-wall amphibole-quartz schist (i.e., metaexhalite). This metaexhalite layer was interpreted based on high iron contents (>25% Fe_2O_3; high magnetic susceptibility) with unique banding features of grunerite- and quartz-rich layers (Kelly et al., 2024). This is in turn overlain by calcite-muscovite-quartz schist (i.e., argillaceous metasedimentary rocks) and garnet amphibolite (i.e., calc-alkaline metabasalt). Additional deeper units of the overturned stratigraphic hanging wall are discussed by Kelly et al. (2024). Intrusions of monzogranite (ca. 2686 Ma; Hollis et al., 2019a) and thin quartz-feldspar porphyry sills crosscut these packages, along with Proterozoic dolerite dikes.

Despite variations in metamorphic grade (greenschist to amphibolite facies) and alteration intensity, the King stratigraphic sequence is broadly consistent along the 45-km strike of the greenstone belt (Fig. 1). Several regional prospects along strike of the King deposit were identified based on soil and airborne Versatile Time Domain Electromagnetic anomalies. Significant drilling intercepts from regional prospects include: (1) King South—6.4 m at 2.4% Zn, 0.86% Pb, and 44 g/t Ag (drill hole EC187D); (2) King North—24 m at 0.1% Zn and 16 m at 0.3% Cu, including 11 m at 0.3% Cu, 0.52 g/t Au, 9 g/t Ag (drill hole EC175D; Kelly et al., 2024; Fig. 1B); (3) EB04 prospect—12 m at 0.18% Cu, 0.1% Zn, 6.4 g/t Ag, and 0.11 g/t Au (drill hole EC195, 7.5 km north of King, Fig 1C); and (4) EB16—3 m at 0.18% Zn (drill hole EC099, Fig. 1D).

The ore mineral assemblages at King have been described in previous studies (Hollis et al., 2019b; Dana et al., 2025) and are summarized as follows. The concordant massive sulfide ore lens (1–7 m thick) is typically composed of recrystallized pyrite with lesser amounts of interstitial pyrrhotite, sphalerite, and chalcopyrite. Marcasite, galena, arsenopyrite, gudmundite (FeSbS), ullmannite (NiSbS), and boulangerite ($Pb_5Sb_4S_{11}$) also occur in the massive sulfide lens in trace amounts. Underlying rocks of the stratigraphic footwall are characterized by discordant veins and disseminated sulfides composed predominantly of pyrite-sphalerite in felsic rocks, and pyrite-chalcopyrite-pyrrhotite with trace amounts of tellurides in the deeper mafic sequence (Dana et al., 2025).

Samples and Analytical Methods

Sampling strategy

Samples were collected from diamond drill hole EC116D from the footwall, massive sulfide lens, and hanging-wall sequences, which was drilled through the center of the King deposit. The compositions of chlorite, white mica, and garnet were analyzed throughout the stratigraphy by electron probe microanalysis (EPMA) and laser ablation-inductively coupled plasma-mass spectrometry (LA-ICP-MS), following traditional petrography and analysis using a scanning electron microscope (SEM). Several representative samples were also collected from the EB04 and EB16 prospects located approximately 7.5 and 30 km north of the King deposit, respectively. Details of drill holes used in this study are provided in Appendix Table A1. These samples were used to test whether the stratigraphic sequences in these prospects exhibit mineral chemical signatures similar to the King deposit, and to aid in stratigraphic interpretations where sampling is limited by air core, rotary airblast, and reverse circulation (RC) drilling.

Petrography

A total of 32 samples consisting of footwall, massive sulfide, hanging-wall, and regional samples were prepared as polished thin sections for mineralogical characterization. Petrographic observations were performed on a Leica DMLP polarizing microscope equipped with a DFC420 C camera. Several representative samples were also further characterized using a Carl Zeiss Sigma HD VP field emission SEM equipped with an Oxford AZtec ED X-ray analysis. The analytical conditions were as follows: accelerating voltage 15 kV, working distance 7 mm, beam current 20 nA, and a pure metallic cobalt standard for calibration.

Whole-rock lithogeochemistry

A total of 24 samples from drill hole EC116D were sent to ALS laboratories at Loughrea, Ireland, for bulk geochemical analysis. Major element contents were determined by four-acid digestion with an inductively coupled plasma-optical emission spectrometry (ICP-OES) finish on fused glass beads. Trace element, HFSE, and rare earth element (REE) contents were determined by lithium borate fusion and an inductively coupled plasma-mass spectrometry (ICP-MS) finish. The base metals (Cu, Pb, Zn, Ni) and trace metals (e.g., As, Sb, Tl, Bi) were analyzed by multiacid digestion, followed by an ICP-OES and an inductively coupled plasma-atomic emission spectrometry (ICP-AES) finish, respectively. Halogen (F and Cl) contents were analyzed using KOH fusion and ion chromatography. Carbon and sulfur were measured by total combustion using a carbon-sulfur analyzer, with loss on ignition (LOI) measured via a robotic thermogravimetric system. Details of whole-rock geochemical data, including the standards used and detection limits, are provided in the Appendix Table A2. Additional geochemical data obtained from a portable X-ray fluorescence spot measurement were also supplied by Geological Survey of Western Australia. The measurement was carried out using an Olympus Innov-X Systems Delta every 4 to 5 m of core, and detailed analytical conditions are those described in Wawryk and Hancock (2022).

EPMA

EPMA was carried out on chlorite, white mica, and garnet using a CAMECA SX100 electron probe microanalyzer at the Grant Institute of the University of Edinburgh. The analytical conditions were as follows: voltage 15 kV; beam current 4 nA and 100 nA for major and minor elements, respectively; beam size 5 µm; and peak measurement time 20 s for major and 30 to 100 s for minor elements (background measurement time is half of peak time; the X-ray line used was Kα for all elements). Several natural minerals were used as standards, including spinel (Mg, Al), wollastonite (Si, Ca), fayalite (Fe), jadeite (Na), orthoclase (K), chromite (Cr), rutile (Ti), halite (Cl), strontiofluorite (F), and pure metal (Zn, Cu, and Mn). Details of the results and lower detection limits are provided in the Appendix Tables A3 to A5. The raw results were processed using ZAF correction. Chlorite, white mica, and garnet were normalized to 28, 11, and 12

oxygens, respectively. For chlorite and white mica, Fe^{2+} is assumed to constitute the total iron (ΣFe), since the estimation of Fe^{3+} by charge balance would require stoichiometric limits to be exceeded, something that is rarely observed in micas and chlorite (Schumacher, 1991; Walters, 2022). For garnet, the estimation of Fe^{2+} and Fe^{3+} was calculated by stoichiometric constraints following the procedures described by Locock (2008).

LA-ICP-MS

Several representative samples were selected for in situ chlorite, white mica, and garnet trace element analysis by LA-ICP-MS at the Brian Price laboratory of the University of Edinburgh. An Analyte Excite 193-nm ArF excimer laser ablation system was used, connected to a Nu Attom high-resolution (HR)-ICP-MS. The laser beam diameter, fluence, and frequency were set at 100 µm, 3.5 J/cm², and 15 Hz, respectively. The ablation time was 30 s with a spot size of 50 µm. The argon flow rate was 0.7 L/min, and the helium (carrier gas) flow rate was 0.8 L/min. The elements were analyzed using linked scan mode at low resolution. The dwell time was 200 µs for 30 cycles at 4 sweeps per cycle. The trace elements were calibrated against the NIST-612 and NIST-610 glass as primary and secondary standards, respectively. The quality of the obtained data was checked by monitoring BCR-2G (Basalt Columbia River) standard with accepted values reference from Jochum et al. (2005). The Mn content, measured by EPMA for each sample, was used for internal standardization. Data reduction was performed in NuQuant v.1.0X AttoLab v.2.11 software coupled with an in-house Microsoft Excel processing spreadsheet. A total of 24 isotopes were measured for chlorite and white mica: ^{7}Li, ^{34}S, ^{45}Sc, ^{49}Ti, ^{51}V, ^{52}Cr, ^{59}Co, ^{60}Ni, ^{63}Cu, ^{66}Zn, ^{75}As, ^{77}Se, ^{85}Rb, ^{88}Sr, ^{111}Cd, ^{115}In, ^{120}Sn, ^{121}Sb, ^{124}Te, ^{133}Cs, ^{138}Ba, ^{205}Tl, ^{208}Pb, and ^{209}Bi. For garnet, a total of 30 isotopes were measured: ^{45}Sc, ^{49}Ti, ^{51}V, ^{52}Cr, ^{63}Cu, ^{66}Zn, ^{88}Sr, ^{89}Y, ^{91}Zr, ^{93}Nb, ^{138}Ba, ^{139}La, ^{140}Ce, ^{141}Pr, ^{146}Nd, ^{147}Sm, ^{153}Eu, ^{157}Gd, ^{159}Tb, ^{163}Dy, ^{165}Ho, ^{166}Er, ^{169}Tm, ^{172}Yb, ^{175}Lu, ^{178}Hf, ^{181}Ta, ^{208}Pb, ^{232}Th, and ^{238}U. Details of LA-ICP-MS results, including the lower detection limits, are provided in the Appendix Tables A6 to A8.

Spectral reflectance

A representative drill hole (EC116D) through the center of the King deposit was scanned using the HyLogger system at the Geological Survey of Western Australia's core library in Perth. The drill core was scanned using both the SWIR and TIR spectrometers, with data analyzed using The Spectral Geologist software. This program compares the spectra produced approximately every 8 mm of core with a database of known minerals and their characteristic absorption features (Hancock et al., 2013; Duuring et al., 2016). For every spectrum produced, the three main minerals contributing to its signature are identified in the TIR and SWIR (Duuring et al., 2016). Chlorite and white mica types are interpreted based on the SWIR absorption features at 2,250 and 2,200 nm, respectively (e.g., Cloutier et al., 2021). Garnet types were interpreted based on the TIR absorption features at 11.3 µm using two different scripts: (1) garnet parameter B (i.e., 11,100W; reflectance peak between 10,850 and 11,300 nm) and (2) garnet parameter T (i.e., 11,300DW; reflectance peak between 11,200 and 11,600 nm; e.g., Izawa et al., 2018; Laukamp et al., 2021).

Results

Whole-rock lithogeochemistry

Downhole whole-rock geochemistry results (Fig. 2; App. Table A2) of the footwall and hanging-wall units from drill hole EC116D are consistent with those reported in previous studies (e.g., Hollis et al., 2019b; Kelly et al., 2024; Dana et al., 2025). The footwall mafic units are characterized by typical tholeiitic basalt affinities (e.g., low Zr/Ti, Th/Yb, and Zr/Y ratios, and high V/Sc and Ti/Nb ratios). Both footwall mafic units have similar Fe/Mg ratios, yet the biotite-muscovite schist has significantly higher Al_2O_3 and alkali ($Na_2O + K_2O$) contents, and lower TiO_2 and MnO than the garnet amphibolite (Dana et al., 2025). Despite having different major element signatures, the footwall felsic units are characterized by typical calc-alkaline dacite-rhyolite affinities (e.g., high Zr/Ti, Th/Yb, and Zr/Y ratios, and low V/Sc and Ti/Nb ratios). Except for the high base metal and S contents, the massive sulfide ore lens has similar geochemical signatures with the upper felsic unit (i.e., upper chlorite-muscovite-quartz schist). The stratigraphically overlying metaexhalite unit is characterized by high Fe contents and displays a pronounced positive Eu anomaly like the underlying massive sulfides (Hollis et al., 2019b). The hanging-wall units, including garnet amphibolite and metasedimentary rocks, are of calc-alkaline affinity, similar to the underlying felsic footwall sequence.

Chlorine contents range from 70 to 430 ppm (Fig. 2), where the highest value is associated with the biotite-muscovite schist, and the lowest values with the upper chlorite-muscovite-quartz schist and footwall garnet amphibolite units. Fluorine contents range from 90 to 1,160 ppm (Fig. 2), with the lower chlorite-muscovite-quartz schist having the highest value, while the lowest values are associated with the amphibole-quartz schist (i.e., metaexhalite) and biotite-muscovite schist units. There is no correlation between bulk F and/or Cl contents with proximity to mineralization.

Chlorite characteristics

Chlorite occurs throughout the stratigraphy and is present within all rock types. Generally, chlorite is more abundant in the mafic units than the stratigraphically higher felsic rocks, though one exception is the thick zones of Mg-metasomatized felsic (i.e., the muscovite-chlorite schist) that occur in the footwall stratigraphy (Fig. 2). Chlorite occurs along the deformation fabrics or as a replacement of prograde metamorphic minerals (e.g., garnet, hornblende, and biotite; Fig. 3). Regardless of its origin and texture, chlorite has similar major and trace element compositions within each sample, and chemical variations are only observed with stratigraphic height or are related to protolith compositions. Most chlorite in the King footwall is predominantly mixed Fe-Mg in composition, although some chlorites from the hanging-wall metaexhalite and deep mafic footwall (i.e., biotite-muscovite schist) plot toward the Fe chlorite end-member field (i.e., chamosite, Mg# <0.3; Fig. 4A). It is also important to note that chlorite hosted by the footwall Mg-metasomatized felsic unit (i.e., muscovite-chlorite schist) at EB04 prospect has a

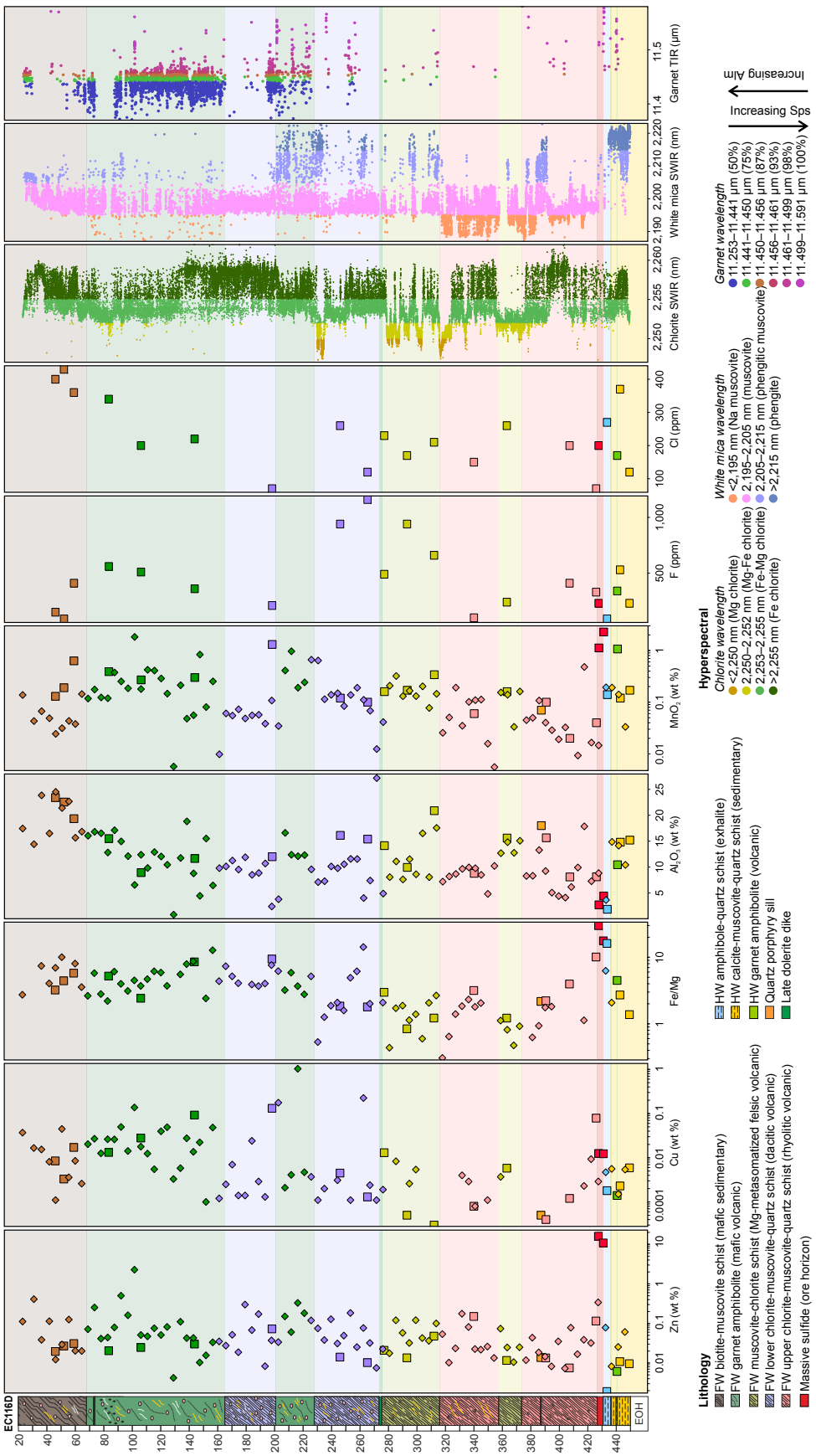

Fig. 2. Downhole geochemistry and hyperspectral signatures of drill hole EC116D. Note that the stratigraphy is overturned. A cross section through the deposit is provided as Appendix Figure A1. Large squares represent whole-rock lithogeochemical analyses, and small diamonds portable X-ray fluorescence data. Abbreviations: Alm = almandine, EOH = end of hole, FW = footwall, HW = hanging wall, Sps = spessartine, SWIR = short-wave infrared, TIR = thermal infrared.

significantly higher Mg content (median Mg# = 0.9) than at King (median Mg# = 0.7).

The Fe and Mg compositions of chlorite at King are generally controlled by the bulk geochemistry of the host rock. This is indicated by the positive correlation between the Mg/(Mg + Fe) ratio of chlorite and $bulk_{molar}$ lithogeochemistry (Fig. 4B), as also discussed by Dana et al. (2025) using whole-rock geochemistry and SWIR data. In contrast, Mn and F contents in chlorite systematically increase with proximity to the massive sulfide lens and then significantly drop in hanging-wall units (Fig. 4C, E). These patterns of increasing Mn and F with stratigraphic height toward the ore lens are also observed in chlorite from the EB04 prospect (Fig. 4). While F contents in chlorite systematically increase toward the ore lens, no such trend is observed for Cl contents (Fig. 4C, D). Similar trending patterns are also observed in the Al content of chlorite, which increases toward the immediate felsic footwall unit and then decreases at the ore horizon and in the hanging-wall units. One exception to this trend is a sample of biotite-muscovite schist (at depth 58 m) where the Al content is significantly lower than the rest of the footwall units (Fig. 4F). This is likely due to the incomplete replacement of biotite by chlorite.

The trace element contents of chlorite at King also vary according to the host lithology and proximity toward the massive sulfide lens. For example, within the footwall, chlorite in mafic units generally contains higher contents of Sc + V + Ni + Co than felsic units (median values of mafic = 661 ppm; felsic = 192 ppm). Overall, chlorite from footwall units is enriched in these elements compared to chlorites from the massive sulfide (median = 41 ppm) and hanging-wall units (median = 19 ppm; Fig. 5C). On the other hand, chlorites from the massive sulfides and hanging-wall units are characterized by higher contents of Rb + Tl + Sr + Cs (median values of footwall units = 2.1 ppm; massive sulfide = 13 ppm; hanging-wall units = 6.9 ppm). Additionally, chlorite from the footwall mafic units is characterized by lower Li contents (median = 27 ppm) compared to the footwall felsic units (median = 66 ppm; Fig. 5D). Chlorite hosted by massive sulfides is also more enriched in several fluid-mobile elements (e.g., Sb, In, Sn, Te, Ba, Pb, Bi, Cd, As, and Cu) compared to the other lithological units in the footwall and hanging wall. It is also important to note that the time-resolved LA-ICP-MS signals (App. Fig. A2), although generally stable, do exhibit minor fluctuations. This may suggest that some of these elements are present as nano-inclusions rather than being structurally incorporated into the chlorite structure.

White mica characteristics

White mica occurs in almost all lithological units at King but was not observed in our samples from the garnet amphibolite, amphibole-quartz schist (i.e., metaexhalite), or massive sulfides. It is commonly found along the main foliation (i.e., regional deformation fabric) and is most abundant in the deep mafic footwall in the biotite-muscovite schist (Fig. 3). Although fine-grained sericite also occurs, it is important to note that only coarse-grained white mica was analyzed in this study. In the footwall stratigraphy, white mica is classified as muscovite and becomes more Na rich ("paragonitic") in the upper chlorite-muscovite-quartz schist unit (i.e., upper felsic; Fig. 6A, B) approaching massive sulfide mineralization. In contrast, all white mica from the hanging-wall stratigraphy is classified as phengite (i.e., solid solution between muscovite, aluminoceladonite, and ferroaluminoceladonite; Fig. 6A).

The major element contents of white mica are relatively homogeneous within individual samples regardless of textural variations (e.g., coarse vs. fine grained). Chemical variations are generally related to the Tschermak ($[Fe^{2+}, Mg]^{VI} + Si^{IV} \leftrightarrow Al^{VI} + Al^{IV}$) and K-Na substitutions. White mica from hanging-wall units is characterized by high Mg (median = 1.6 wt %) and Ca (median = 0.2 wt %) but low Al (median = 14 wt %) contents, although several footwall felsic units also show enrichment in Mg (up to 1.2 wt % in muscovite-chlorite schist) and Ca (up to 0.3 wt % in lower chlorite-muscovite-quartz schist). As also observed for chlorite, F contents of white mica also increase systematically toward the massive sulfide lens in the footwall units and then are lower in immediate hanging-wall units (Fig. 6C). High contents of F in white mica (up to 3,000 ppm) were also obtained in felsic rocks of the EB04 prospect.

In terms of trace elements, white mica from the hanging-wall rocks is characterized by significantly lower Ba (median = 51 ppm), Rb (median = 8.7 ppm), and Tl (median = 0.1 ppm) but higher Sr (median = 67 ppm) contents compared to white mica from the footwall units (median values of Ba = 634 ppm; Rb = 158 ppm; Tl = 0.7 ppm; Sr = 17 ppm; Fig. 7A-C). Additionally, the footwall upper felsic unit that occurs stratigraphically below the massive sulfide also shows significantly higher Tl (median = 17 ppm) and Li (median = 150 ppm) contents. White mica in the footwall felsic units is also more enriched in Cs (median = 6.8 ppm) compared to footwall mafic (median = 0.8 ppm) and hanging-wall units (median = 0.8 ppm). Several trace elements also show increasing contents with proximity to the massive sulfides in the uppermost footwall stratigraphy. For example, Sc + Ti in the uppermost footwall increases while S decreases toward the massive sulfide lens (Fig. 7E, F).

Garnet characteristics

Garnet occurs throughout the stratigraphy, most commonly as porphyroblasts. It is more abundant in the footwall mafic units and less abundant in the stratigraphically higher footwall felsic units. Garnet commonly hosts small inclusions (e.g., quartz and ilmenite) and is locally replaced by secondary chlorite (Fig. 3D). Inclusions of sphalerite, galena, and pyrrhotite are also common in garnet within the massive sulfide lens.

The major element composition of garnet within the footwall is relatively consistent, whereas garnets hosted by the massive ore lens and hanging-wall units display distinct differences. Regardless of the host lithology, the garnet composition hosted by footwall and hanging-wall units is dominated by the almandine end member ($Alm_{35–87}Sps_{1–53}Prp_{2–17}Grs_{1–31}$, where Alm = almandine, Sps = spessartine, Prp = pyrope, and Grs = grossular), with hanging-wall units having an increased grossular end-member component (Fig. 8). Similar garnet compositions are also observed in those from the felsic and mafic footwall of the regional prospects. Garnet hosted within the massive sulfide lens is distinguished by its higher Mn content ($Sps_{34–52}$) compared to footwall ($Sps_{2–23}$) and hanging-wall ($Sps_{11–24}$) garnets. A narrow Mn-rich band was observed at the rim of some garnet porphyroblasts hosted by massive sulfide.

Several trace elements also show differences between

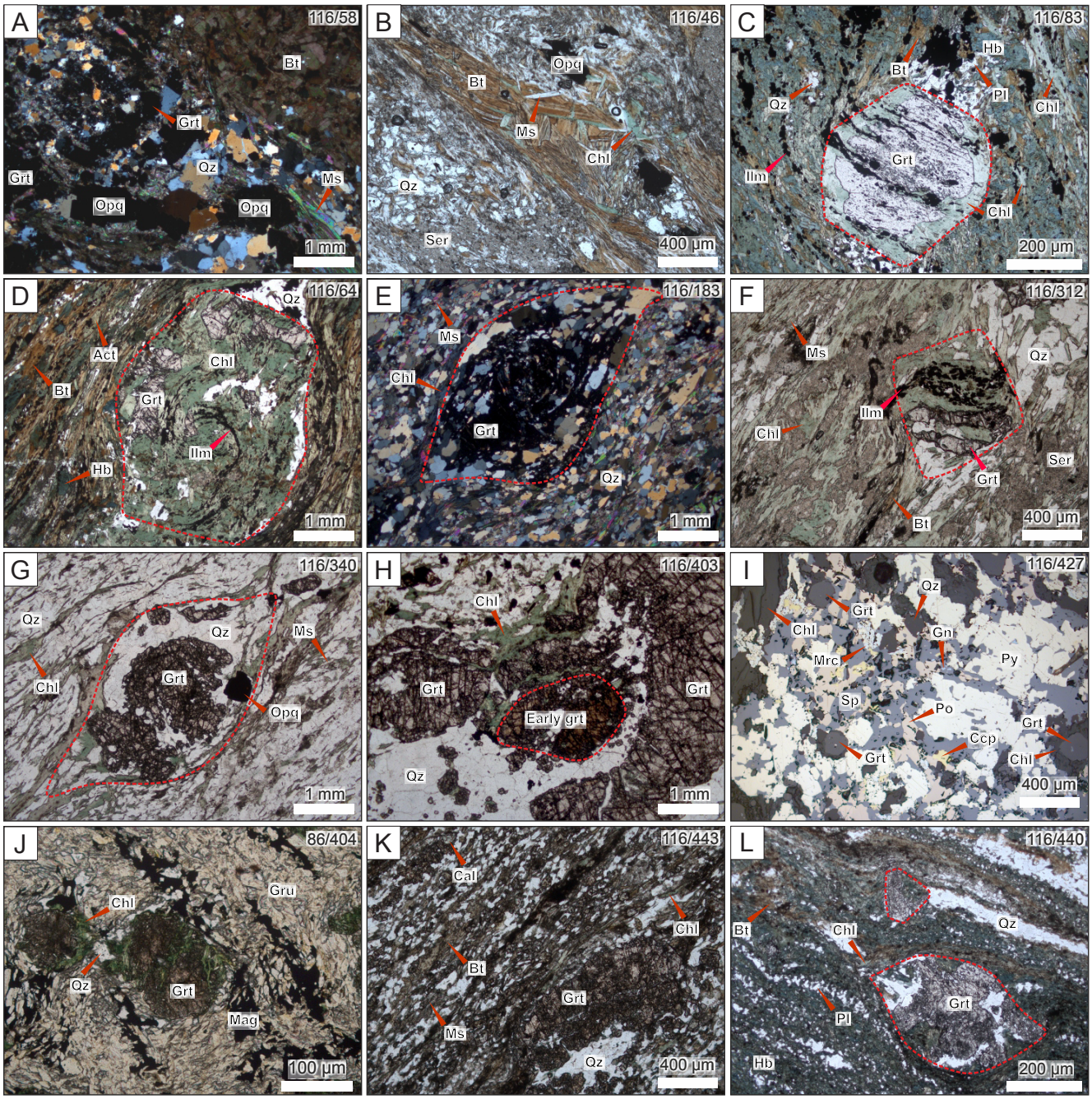

Fig. 3. Photomicrographs of footwall and hanging-wall units from the King deposit highlighting the mode of occurrences of chlorite, white mica, and garnet: (A, B) footwall biotite-muscovite schist; (C, D) footwall garnet amphibolite; (E) footwall upper chlorite-muscovite-quartz schist; (F) footwall muscovite-chlorite schist; (G, H) footwall upper chlorite-muscovite-quartz schist; (I) massive sulfide; (J) hanging-wall amphibole-quartz schist; (K) hanging-wall calcite-muscovite-quartz schist; (L) hanging-wall garnet amphibolite. Mineral abbreviations: Act = actinolite, Bt = biotite, Cal = calcite, Ccp = chalcopyrite, Chl = chlorite, Gn = galena, Grt = garnet, Gru = grunerite, Hb = hornblende, Ilm = ilmenite, Mag = magnetite, Mrc = marcasite, Ms = muscovite, Opq = opaque minerals, Pl = plagioclase, Po = pyrrhotite, Py = pyrite, Qz = quartz, Ser = sericite, Sp = sphalerite.

garnets from the footwall and hanging wall of the King deposit. For example, footwall garnet has higher V (median = 36 ppm) but lower Sr (median = 0.05 ppm) contents compared to hanging-wall garnet (median values of V = 6.1 ppm; Sr = 1.4 ppm) (Fig. 9). At King, there are no significant trace element differences between garnet hosted by footwall mafic and felsic units, except Ti from the garnet amphibolite is significantly higher (median = 202 ppm) compared to other footwall units (median = 83 ppm). Titanium enrichment is evident in garnets from both regional mafic and felsic units. A distinction between footwall- and hanging-wall-hosted garnets was also observed in REE patterns (Fig. 10). Garnets from the

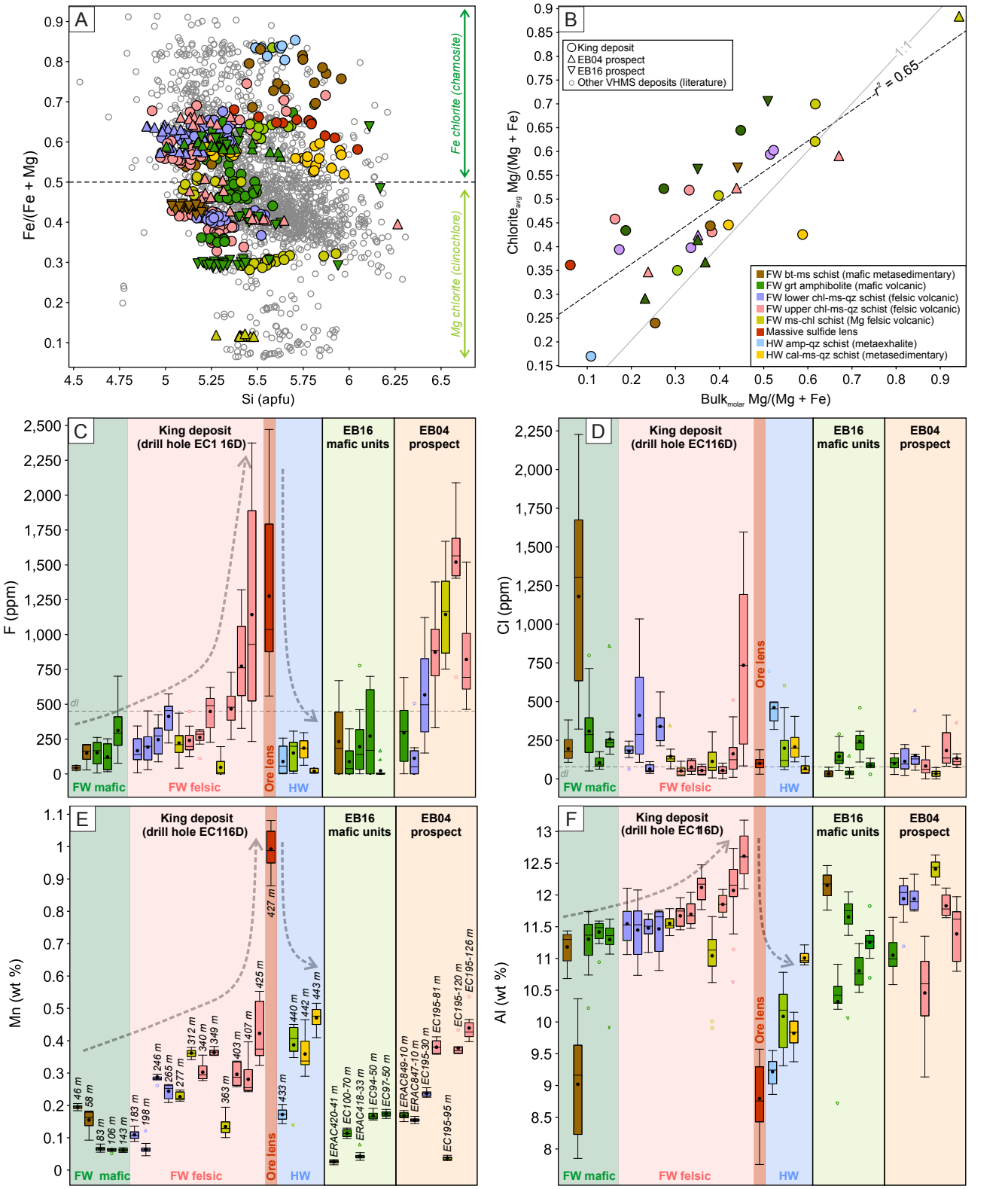

Fig. 4. Chemical characteristics of chlorites from the King deposit and surrounding regional prospects (i.e., EB04 and EB16): (A) chlorite (trioctahedral) discrimination diagram after Zane and Weiss (1998); (B) positive correlation between Mg/(Mg + Fe) in chlorite with bulk$_{molar}$ Mg/(Mg + Fe) of the host lithology; (C-F) downhole F-Cl-Mn-Al contents from drill hole EC116D and regional prospects. Literature data compiled from Yeats et al. (2017) and references therein. Abbreviations: amp = amphibole, apfu = atoms per formula unit, bt = biotite, cal = calcite, chl = chlorite, FW = footwall, grt = garnet, HW = hanging wall, ms = muscovite, qz = quartz, VHMS = volcanic-hosted massive sulfide.

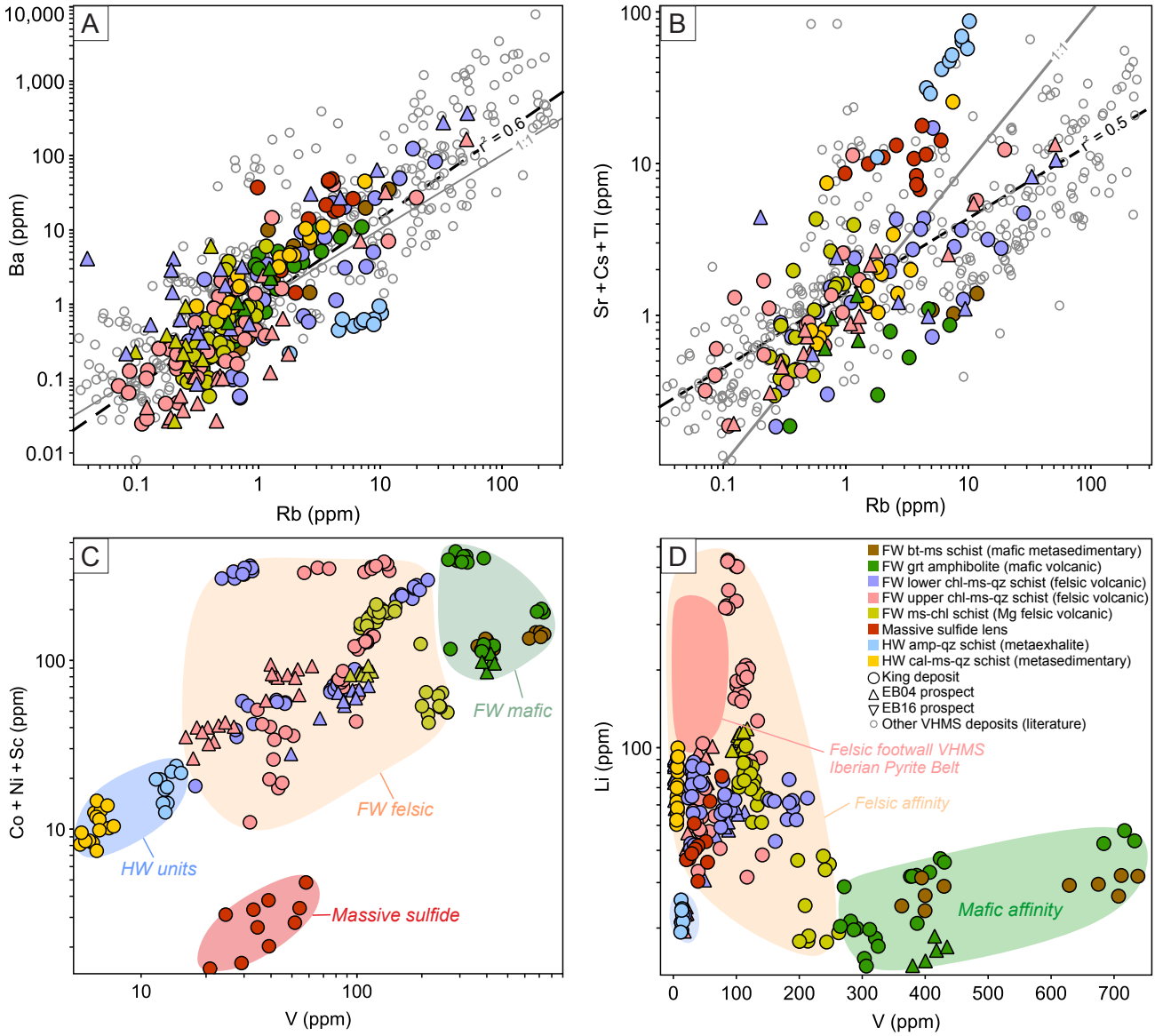

Fig. 5. Trace element chemical variation of chlorites from the King deposit and surrounding regional prospects: (A, B) positive correlation between Rb versus Ba and Sr + Cs + Tl; (C, D) vanadium versus Co + Ni + Sc and Li contents highlighting the affinity of the host rock (i.e., felsic vs. mafic). Literature data compiled from Gisbert et al. (2022) and Soltani Dehnavi et al. (2019). Abbreviations: amp = amphibole, bt = biotite, cal = calcite, chl = chlorite, FW = footwall, grt = garnet, HW = hanging wall, ms = muscovite, qz = quartz, VHMS = volcanic-hosted massive sulfide.

footwall units and massive sulfide lens generally show similar REE patterns. These are characterized by depletion in the light rare earth elements (LREEs), a positive Eu anomaly, and flattish HREE profiles. These patterns also occur in garnets from the regional EB04 felsic and mafic units, although the positive Eu anomaly is less prominent or can be absent. In contrast, hanging-wall garnet shows depletion in the LREEs, lacks a positive Eu anomaly, and is more enriched in the HREEs. Another common signature is the presence of a weak negative Ce anomaly in most units at King (Fig. 10). At the regional EB04 prospect, garnet amphibolite is characterized by a strong negative Ce anomaly, whereas the upper felsic lacks a negative anomaly.

Hyperspectral signatures (chlorite-white mica-garnet)

Spectral signatures of chlorite, white mica, and garnet are plotted in Figure 2 with respect to the King stratigraphy. The downhole trends of chlorite and white mica SWIR signatures from drill hole EC116D are consistent with general trends across the King deposit described recently by Dana et al. (2025). Chlorite SWIR signatures (2,250W) are dominated by mixed Fe-Mg chlorite compositions, with shift toward Mg-rich chlorite in the muscovite-chlorite schist, and Fe-rich chlorite in more Fe-rich rocks. The latter include the metaexhalite, deep mafic rocks of the footwall stratigraphy (e.g., biotite-muscovite schist), and sulfide-bearing felsics (i.e., upper chlorite-muscovite-quartz schist). White mica

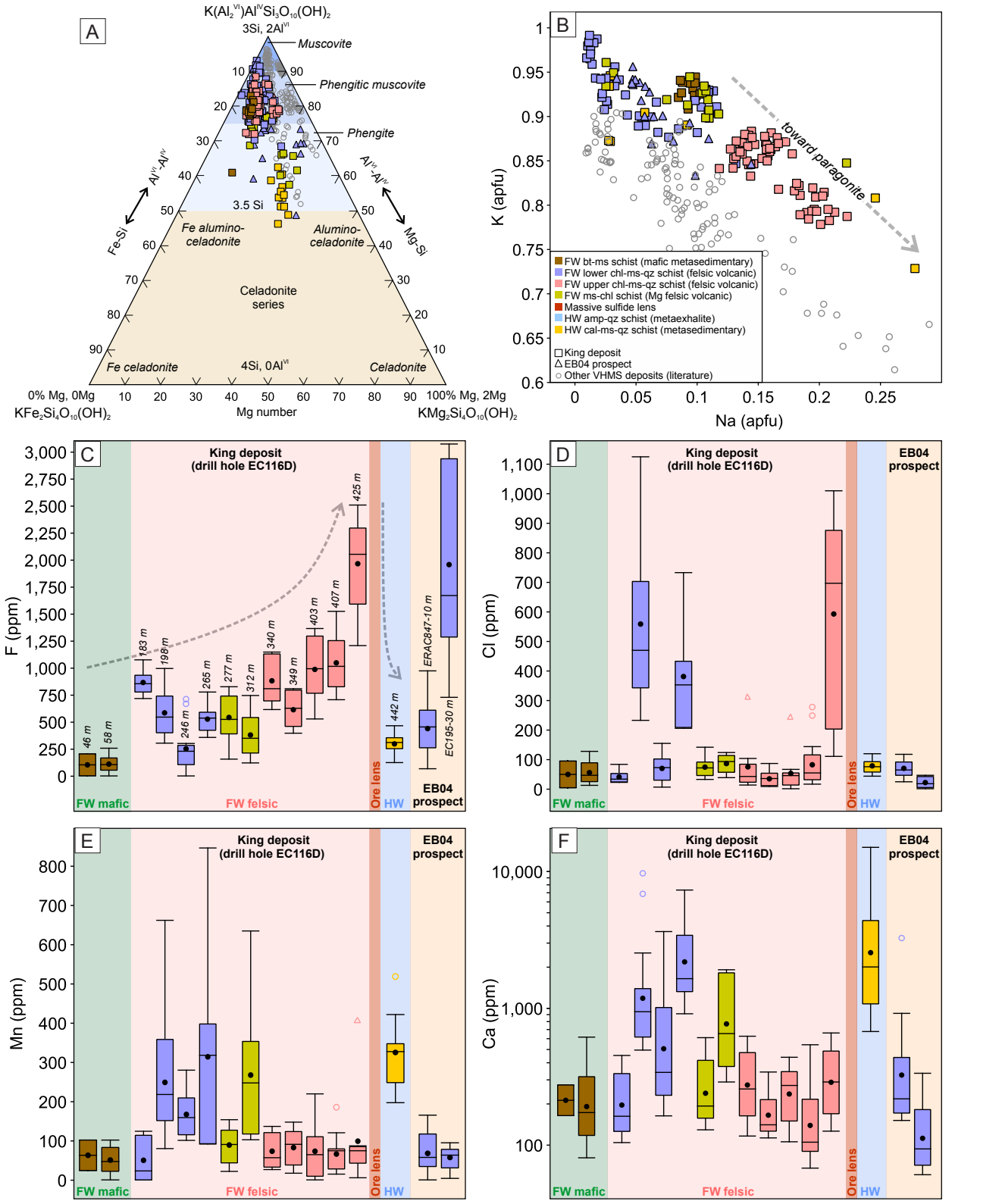

Fig. 6. Chemical characteristics of white micas from the King deposit and EB04 prospect: (A) ternary diagram showing muscovite, celadonite, and Fe celadonite end members (modified after Tappert et al., 2013); (B) negative correlation between Na versus K contents of white mica; (C-F) downhole chemical variation of white micas from drill hole EC116D and regional prospect EB04. Literature data compiled from Gisbert et al. (2022) and Soltani Dehnavi et al. (2018, 2019). Abbreviations: amp = amphibole, apfu = atoms per formula unit, bt = biotite, cal = calcite, chl = chlorite, FW = footwall, HW = hanging wall, ms = muscovite, qz = quartz, VHMS = volcanic-hosted massive sulfide

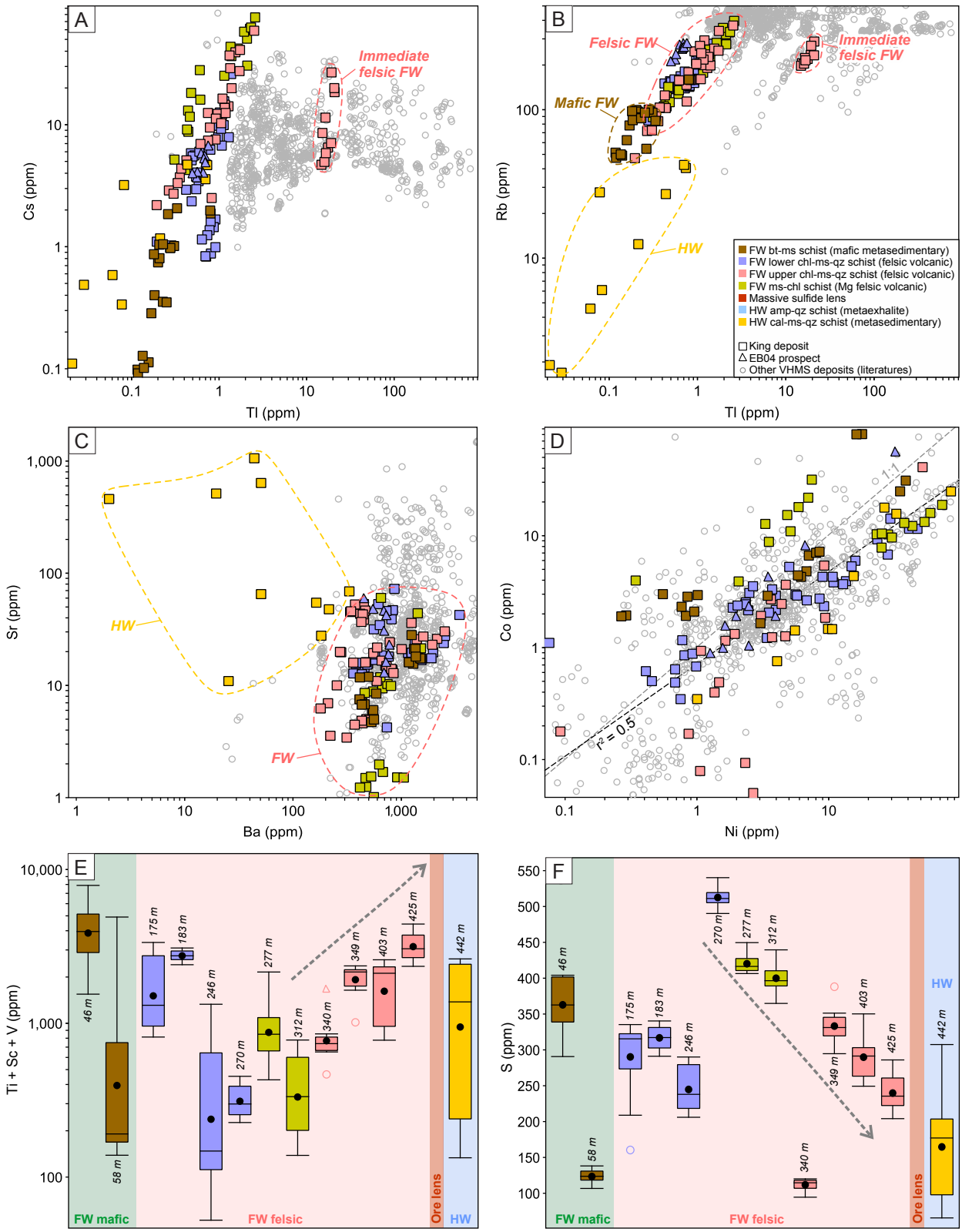

Fig. 7. Trace element chemical variation of white micas from the King deposit and EB04 regional prospect: (A, B) positive correlation between Tl versus Cs (r^2 = 0.4) and Rb (r^2 = 0.5) contents; (C) Ba versus Sr content highlighting the distinction between white micas from the footwall and hanging wall; (D) positive correlation between Ni versus Co; (E, F) downhole Ti + Sc + V and S contents of white mica from drill hole EC116D. Literature data compiled from Gisbert et al. (2022) and Soltani Dehnavi et al. (2018, 2019). Abbreviations: amp = amphibole, bt = biotite, cal = calcite, chl = chlorite, FW = footwall, HW = hanging wall, ms = muscovite, qz = quartz, VHMS = volcanic-hosted massive sulfide.

SWIR signatures are dominated by muscovite throughout the footwall and become more phengitic in hanging-wall units. A shift toward the Na muscovite wavelength is observed in the footwall upper chlorite-muscovite-quartz schist that forms the immediate footwall to massive sulfides. Minor shifts to phengitic wavelengths in footwall units (e.g., garnet amphibolite at 200–230 m; Fig. 2) are associated with high Fe and/or Mg whole-rock contents, reflected by high carbonate-chlorite-pyrite index values (Dana et al., 2025).

The mineral-chemical trends identified through EPMA align with those traditionally observed using reflectance spectroscopy. The 2,200W feature of white mica correlates positively with Si (r^2 = 0.6) and Mg (r^2 = 0.9) contents in white mica, and negatively with Al contents (r^2 = 0.7) (App. Fig. A3). These trends commonly observed in white mica are traditionally associated with Tschermak substitution (e.g., Cloutier et al., 2021, and references therein). Apart from the phengite wavelength (i.e., >2,215 nm), the 2,200W also positively correlates with the average of Ni, Co, and Zn contents (r^2 = 0.4–0.5). The 2,250W feature of chlorite correlates positively with Fe/(Fe + Mg) (r^2 = 0.4) contents of chlorite (App. Fig. A4). This is typical for signatures of trioctahedral chlorite (e.g., Cloutier et al., 2021). The 2,250W feature also correlates negatively with V + Cr contents (r^2 = 0.5) (App. Fig. A3).

TIR HyLogger data show that garnet is most abundant in the garnet amphibolite unit and becomes rarer in the stratigraphically overlying felsic sequence. The 11,100W and 11,300DW are positively correlated (r^2 = 0.6), and both are negatively correlated with the almandine content of garnet (r^2 = 0.7; App. Fig. A5). Conversely, these absorption features positively correlate with the spessartine content of garnet (r^2 = 0.6). The downhole garnet TIR data show that the footwall mafic units are dominated by the almandine end member and shift toward more spessartine in the footwall felsic units, which is consistent with EPMA results. Additionally, the 11,100W feature also shows positive correlation with HFSE (r^2 = 0.8) and Ba + Sr contents (r^2 = 0.7).

Discussion

Mineral chemical vectors toward massive sulfide mineralization

Fluorine in chlorite and white mica: Although several studies have been conducted to understand the chemical variations of chlorite and white mica in VHMS deposits, most of these studies were undertaken in low-grade metamorphic terranes where the original alteration mineralogy is still preserved (e.g., Laakso et al., 2016; Soltani Dehnavi et al., 2018; Hollis et al., 2021; Gisbert et al., 2022). In high-grade metamorphic terranes, it is important to understand whether the chemical variation in preserved mineral assemblages still reflects the hydrothermal alteration signatures prior to metamorphism or

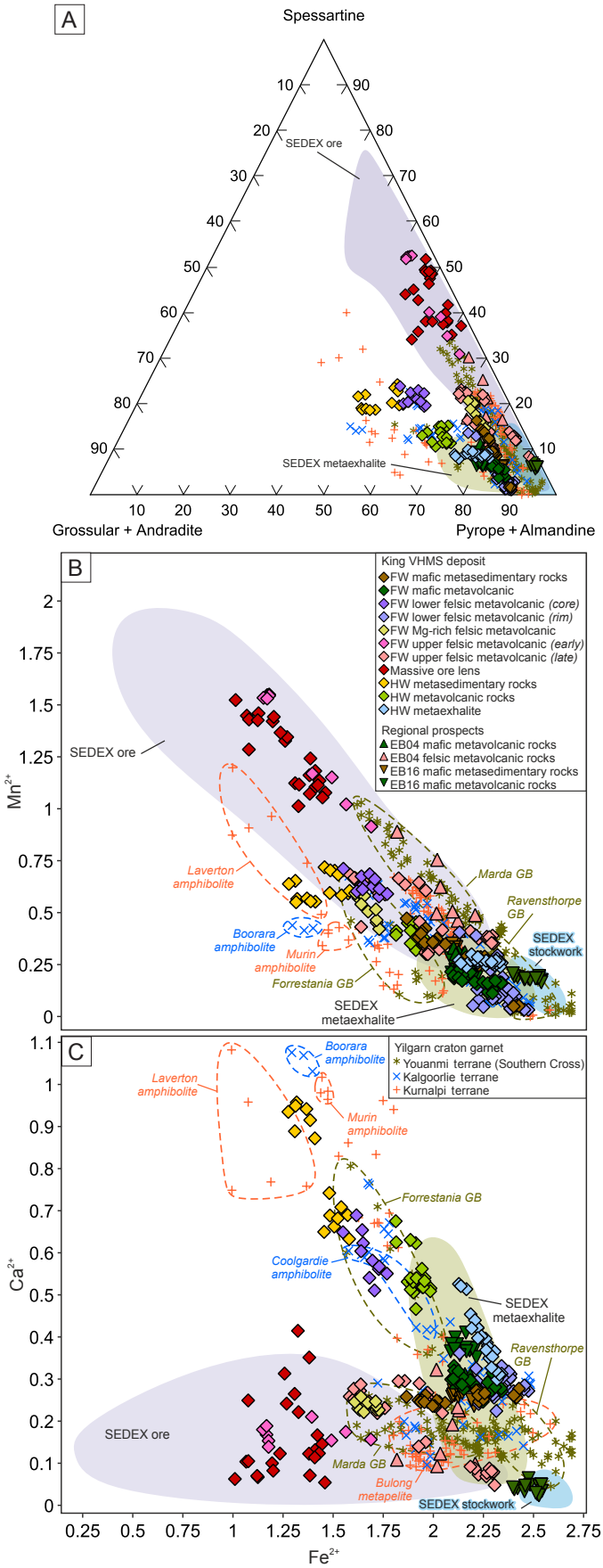

Fig. 8. Major element chemical characteristics of garnets from the King deposit and surrounding prospects: (A) garnet end member ternary diagram; (B, C) Fe versus Mn and Ca contents of garnet. Literature data compiled from SEDEX (Heimann et al., 2013; Pollock et al., 2018; Tott et al., 2019; Lisboa et al., 2023), Yilgarn (Goscombe et al., 2009, 2019). Abbreviations: FW = footwall, GB = greenstone belt, HW = hanging wall, SEDEX = sedimentary exhalative, VHMS = volcanic-hosted massive sulfide.

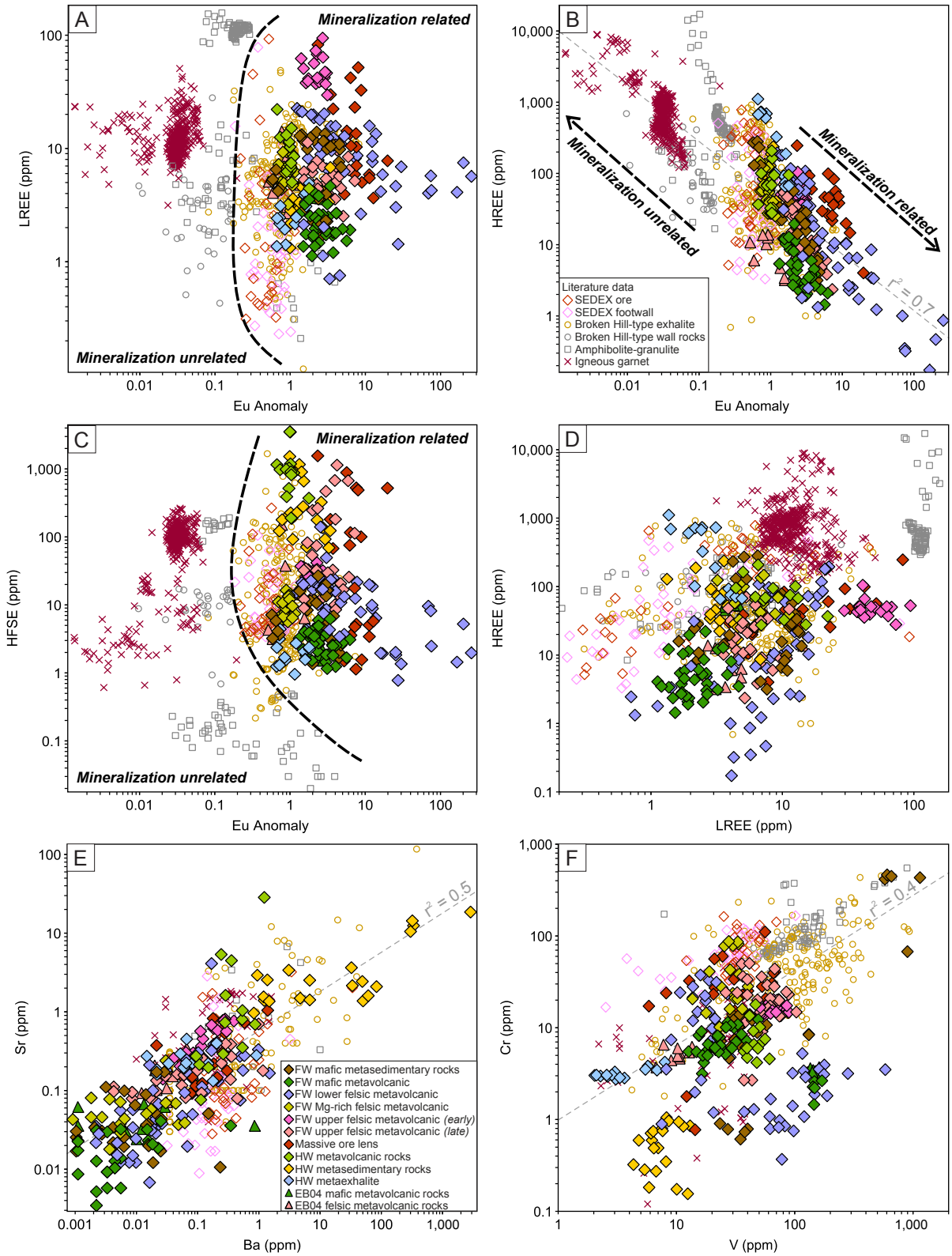

Fig. 9. REE and trace element variation of garnet highlighting the distinction between garnets associated with mineralization and those from barren metamorphic and igneous rocks: (A-C) Eu anomaly versus total REE and HFSE contents; (D) HREE versus LREE; (E) Ba versus Sr; and (F) V versus Cr. Literature data compiled from SEDEX (Heimann et al., 2013; Pollock et al., 2018; Tott et al., 2019; Lisboa et al., 2023); Broken Hill (Spry et al., 2007; Heimann et al., 2011); amphibolite-granulite metamorphic rocks (Bea et al., 1997; Tual et al., 2021); igneous garnet (Lucci et al., 2018; Cravinho et al., 2024). Abbreviations: FW = footwall, HFSE = high field strength element, HREE = heavy rare earth element, HW = hanging wall, LREE = light rare earth element, REE = rare earth element, SEDEX = sedimentary exhalative.

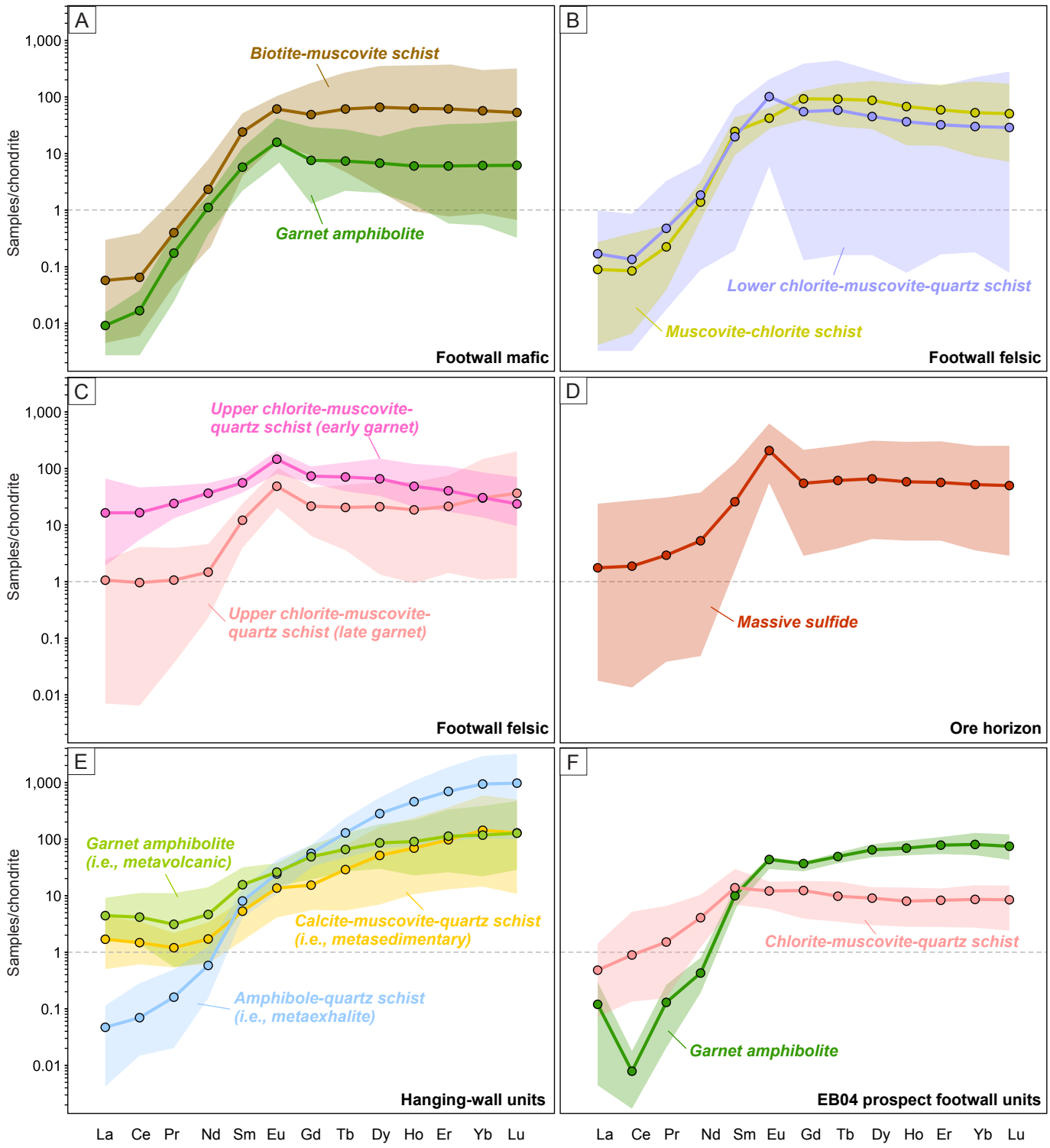

Fig. 10. Chondrite-normalized REE pattern of garnets from the (A) mafic footwall, (B, C) felsic footwall, (D) massive sulfide lens, (E) hanging-wall units of the King deposit, as well as (F) representative data from EB04 prospect. Chondrite normalization values from McDonough and Sun (1995). Abbreviation: REE = rare earth element.

has been modified and obscured during later recrystallization and metal remobilization.

Previous studies have suggested that Fe/(Fe + Mg) variation in ferromagnesian silicates (including chlorite and white mica) is attributed to the effect of sulfur and oxygen fugacity, in which the Fe/(Fe + Mg) ratio decreases with proximity to the massive sulfides (e.g., Nesbitt, 1982; Spry, 1998). However, the effect of sulfidation and oxidation on the chlorite

and white mica compositions seems to be minimal at King. A previous study at King by Dana et al. (2025) using bulk geochemistry and SWIR data suggested that chlorite chemistry is strongly controlled by bulk-rock Fe/Mg composition with a minor influence of Mn of the host lithology prior to metamorphism. This reflects a combination of both the original protolith composition (i.e., a switch from mafic to felsic volcanism with stratigraphic height) and, more importantly, the intensity of Mg and Fe metasomatism of these rocks by hydrothermal alteration that controls their Fe/Mg ratio. This strong bulk geochemical control on chlorite chemistry is consistent with a positive correlation between Mg/(Mg + Fe) of chlorite and its host lithology (Fig. 4B). Our study shows that while Fe/Mg ratios in chlorite are not particularly useful as a vectoring tool in VHMS deposits metamorphosed to the amphibolite facies (except for delineating zones of intense Mg metasomatism as potential fluid pathways), several trace elements have significant value for exploration. EPMA of chlorite in the host stratigraphy demonstrates that F and Mn contents systematically increase through the footwall units toward the massive sulfide lens and then dramatically drop in the hanging-wall units. Similar patterns are also observed for the contents of F in white mica and Mn in garnet.

The behavior of F in VHMS systems is still relatively poorly understood (e.g., Reeves et al., 2011; Kendrick, 2018). The lack of any correlation between F with Mg and Fe in chlorite, as well as with the bulk F content of the host lithology, suggests that this F trend is not simply a reflection of iron avoidance in the chlorite structure (Munoz, 1984). Although felsic magmas and their exsolved fluids are globally enriched in F (e.g., Carroll and Webster, 1994; Yang and Scott, 2006; Aiuppa et al., 2009), the systematic increase of F toward massive sulfide at King is most likely due to metasomatism from hydrothermal fluids. This increase occurs throughout all rock types, regardless of protolith composition, alteration style, or intensity. A study of the Kristineberg deposit (Sweden) by Hannington et al. (2003) reported similar patterns, where chlorite in proximity to the massive sulfide lens is enriched in F and Mn. Additionally, several other studies have also demonstrated the association of high F contents both in chlorite (e.g., Iberian Pyrite Belt; Gisbert et al., 2022) and bulk geochemistry within the felsic footwall of other VHMS districts (e.g., Lavery, 1985; Koopman et al., 1999). The systematic enrichment of F in chlorite is not reflected in the bulk content of the host lithology (Fig. 2). This is because F preferentially partitions into several minerals, including (in preferential order) apatite, titanite, biotite, and amphibole (e.g., Hammerli and Rubenach, 2018), whereas chlorite and white mica are less favorable hosts. Consequently, the bulk F content depends largely on the modal abundance of these preferred minerals within the rock.

Hannington et al. (2003) suggested that the F enrichment toward massive sulfides could be attributed to the metasomatism prior to metamorphism, which is consistent with its behavior in modern sea-floor hydrothermal systems. Several studies suggest that the halogen enrichment in metamorphic minerals can be a direct preservation of the initial halogen content in the protolith (e.g., Markl et al., 1997; Yardley and Graham, 2002). It was suggested by Selverstone and Sharp (2015) that primary heterogeneities of halogen contents in the protolith persist throughout metamorphism, with F becoming recycled into newly formed or recrystallized mineral phases rather than being released into devolatizing fluids. Since F concentrations in metamorphic fluids are generally low (e.g., Yardley, 1996) and the fluid-rock interaction during metamorphism is likely limited (e.g., Hammerli et al., 2014), the effect of regional metamorphism on the original F variation associated with VHMS alteration was likely negligible. If F-bearing fluids were introduced later by metamorphism, they would not significantly affect chlorite and white mica, as F would preferentially be incorporated into other minerals.

While the systematic trend of increasing F toward massive sulfide mineralization was observed both in chlorite and white mica, this is not the case with Cl contents. This is consistent with previous studies suggesting that F varies independently of Cl in vent fluids (e.g., Edmond et al., 1979; Gieskes et al., 2002; James et al., 2014) and is preferably partitioned into fluids during high-grade metamorphism (Zhu and Sverjensky, 1991). Chlorine enrichment in chlorite and white mica occurs in the felsic footwall immediately below the massive sulfide. This is likely due to infiltration of halogen-rich fluids such as seawater (e.g., Quinby-Hunt and Turekian, 1983; Kendrick, 2018). Regardless, chlorite and white mica are only enriched in Cl when biotite is absent or when they replaced biotite. Bulk-rock Cl contents generally correspond to the modal abundance of biotite and amphibole, as Cl is preferentially incorporated in these minerals in amphibolite-granulite facies rocks when apatite is rare or absent (e.g., Hammerli et al., 2014; Hammerli and Rubenach, 2018).

Manganese in chlorite and garnet: At King, systematic increases in the Mn content of chlorite and garnet occur with proximity to massive sulfide mineralization in the footwall stratigraphy. Previous studies (e.g., Hannington et al., 2003; Mercier-Langevin et al., 2007) have also reported Mn enrichment in these minerals around massive sulfide deposits. Although chlorite forms as a result of metamorphism, either through the recrystallization of early hydrothermal chlorite or as a product of retrograde metamorphism, its composition is largely influenced by the bulk chemistry of the host rock prior to these events (Dana et al., 2025). Since the precursor rock is enriched in Mn, the resulting metamorphic mineral assemblages also exhibit Mn enrichment.

Previous studies have suggested that Mn-rich garnet can form through the reaction of Mn-rich carbonate with clay minerals such as kaolinite or pyrophyllite (Plimer, 2006; Heimann et al., 2009). Manganese was most likely originally sourced from leached basaltic rocks at depth through alteration by hydrothermal fluids (Kimberley, 1989). In VHMS systems, high-temperature silicate alteration at depth involves interactions between volcanic rocks and hot, acidic seawater-derived hydrothermal fluids. This intense hydrothermal alteration leads to the depletion of elements such as Fe, Ca, Si, Cu, and Mn in the source region (e.g., Galley, 1993; Perfit et al., 1997; Franklin et al., 2005; Jowitt et al., 2012). These elements are then transported by hydrothermal fluids during up-flow, resulting in extensive low-temperature Fe-Si-Mn alteration around the ore horizon, which can be correlated with the chemistry of secondary minerals such as chlorite, smectite, and kaolinite (e.g., Galley, 1993; Perfit et al., 1997; Franklin et al., 2005). The process is commonly accompanied by the precipitation of Fe-Mn oxides and Mn-rich carbonates (e.g., Franklin et al., 2005;

Hannington, 2014). As will be discussed below, Mn-Ca-Fe contents in garnet also provide a useful discriminant between footwall and hanging-wall rocks for regional exploration.

We suggest that together, F and Mn contents in chlorite and/or white mica can be used to delineate zones of hydrothermal up-flow in metamorphosed VHMS systems globally (e.g., Seyfried and Ding, 1995; Hannington et al., 2003; Kendrick, 2018), and those systematic variations can be used to vector toward massive sulfide mineralization. As demonstrated in this study, the vertical extent of the F and Mn chemical alteration halo reaches up to 200 m (Figs. 4, 6), comparable to the vertical extent reported in the Iberian Pyrite Belt, which can reach up to 300 m (Gisbert et al., 2022). It is important to note that the lateral extent of the associated alteration halo (i.e., from proximal to distal along strike) remains untested at King. However, a previous study by Hannington et al. (2003) suggested that magnesium-rich chlorite alteration, enriched in F and Mn, can extend laterally up to ~2 km.

Petrologic discrimination in high-grade metamorphic terranes

Identifying protolith affinity: At King, several trace elements in chlorite are also found to be useful to discriminate the protolith affinity. For instance, Li, V, Sc, Co, and Ni contents in chlorite have a strong association with the affinity of the host lithology (i.e., mafic vs. felsic lithologies; Fig. 5C, D). Vanadium and Sc are generally regarded as immobile during hydrothermal alteration, making them reliable indicators of precursor rock composition (e.g., Halley et al., 2016; Zivkovic et al., 2024). While Li can be mobile under certain conditions, its concentration in VMS-related hydrothermal fluids is typically very low (~2 ppm; e.g., Reyes and Trompetter, 2012; Cai et al., 2024), minimizing its impact on chlorite composition. Moreover, even in cases of Li enrichment, the element tends to partition preferentially into coexisting minerals such as staurolite, cordierite, biotite, muscovite, garnet, and tourmaline (in that order; Dutrow et al., 1986), rather than chlorite. Therefore, Li contents in chlorite are likely to reflect precursor mineral signatures rather than hydrothermal alteration. Cobalt and Ni can be introduced during hydrothermal alteration, but they are typically incorporated into sulfides or Ni-Co-bearing minerals (e.g., cobaltite, ullmannite, pentlandite), all of which are observed at King (Dana et al., 2025). Their limited incorporation into chlorite further supports the interpretation that Co and Ni contents in chlorite are inherited from precursor phases such as retrograde garnet, amphibole, or biotite, or from earlier-formed chlorite that has recrystallized. Altogether, the geochemical signatures of V, Sc, Li, Co, and Ni in chlorite are interpreted to largely reflect the original lithological composition, rather than later fluid-rock interactions. Furthermore, the strong lithological control on these elements, despite amphibolite facies overprinting, suggests that metamorphism has not significantly altered their trace element distribution in chlorite (Gisbert et al., 2022).

Interestingly, we observed a number of potential correlations between spectral reflectance features in chlorite and trace element chemistry that may be useful for photolith discrimination. For instance, the absorption feature of chlorite (2,250W) shows a negative correlation with V (+ Cr) contents (r^2 = 0.5; App. Fig. A4), which we have demonstrated to be useful to distinguish mafic from felsic units (Fig. 5C, D). This correlation probably corresponds to the R^{3+} substitutions in chlorite (Wiewiora and Weiss, 1990). No trace elements were observed in white mica that were able to distinguish protolith affinity, although the 2,200W feature is positively correlated with Co (r^2 = 0.5; App. Fig. A5) and weakly with Ni and Zn (r^2 = 0.4). This correlation is probably associated with R^{2+} substitutions (DeVries and Roy, 1958). Further investigations are required to evaluate these relationships.

Distinguishing VHMS footwall and hanging-wall units: Distinguishing between footwall and hanging-wall units is critical for the effective exploration of VHMS deposits. This is due to their stratiform nature, clustering along stratigraphic horizons within camps, and the need for exploration personnel to determine whether the ore horizon has been adequately tested during regional drilling campaigns. Delineating the ore horizon is particularly challenging when exploring in high-grade metamorphic terranes, where extensive recrystallization and mineral transformation has obscured the original alteration assemblages. Moreover, as similar lithological units can also occur both in the footwall and hanging-wall stratigraphy, these might be difficult to distinguish from rock chips obtained by regional RC drilling. This is particularly the case at King, where units of garnet amphibolite unit can be found in the footwall and hanging-wall sequences. The creation of robust mineral chemical indicators for identifying the ore horizon and discriminating between footwall and hanging-wall rocks is required.

Previous research at King using SWIR hyperspectral data suggests that white mica chemistry can be useful to distinguish between footwall and hanging-wall assemblages. Footwall mafic units are characterized by muscovitic white mica that becomes more Na rich in the felsic footwall immediately below the massive sulfide lens, whereas the hanging wall is dominated by phengitic white mica (Dana et al., 2025). This is also supported by microprobe compositions from this study that generally show similar results (Fig. 6A, B). As suggested by previous studies, the association of phengitic mica in hanging-wall units is attributed to either its high-Fe whole-rock content (i.e., magnetite-rich metaexhalite; Dana et al., 2025) or its Mg-rich seawater entrainment and Ca-Mg carbonate alteration prior to metamorphism (e.g., Thompson et al., 2009; Yang et al., 2011; Gisbert et al., 2022). In terms of trace element contents, white mica in the footwall units is characterized by lower Sr but higher Ba and Rb contents than that in the hanging-wall units. The enrichment of Ba and Rb in white mica is typical of proximal zone signatures of VHMS systems, which also have been reported in several VHMS districts (e.g., Iberian Pyrite Belt, Gisbert et al., 2022; Bathurst mining camp, Soltani Dehnavi et al., 2018). Although white mica is relatively resistant to weathering and can be preserved within the regolith and saprock horizons (e.g., Wilson, 2004; Ehara Suryantini et al., 2005; Salama et al., 2025), the position of its main absorption feature (2,200W) can shift during weathering. Caution is therefore required when interpreting SWIR data obtained from weathered rock.

Both EPMA and SWIR data suggest that chlorite type is fairly similar throughout the stratigraphy, although a shift toward Mg-rich chlorite is observed in the Mg-metasomatized felsic unit. Chlorite from the hanging-wall metaexhalite unit

is also characterized by the Fe-chlorite end member (i.e., chamosite). The main distinction between footwall and hanging wall in terms of chlorite chemistry is the Al content—the footwall generally has higher Al contents than those in the ore lens and hanging-wall stratigraphy. The observed Al trend may reflect hydrothermal temperature gradients (e.g., empirical chlorite geothermometer; Zang and Fyfe, 1995), which is consistent with models of hydrothermal fluid up-flow in VHMS systems (e.g., Galley, 1993; Franklin et al., 2005). However, as the region has undergone amphibolite facies metamorphism (500°–700°C; Goscombe et al., 2019), this may have overprinted or reequilibrated the original chlorite temperatures. As chlorite is highly susceptible to weathering and often vanishes even in mildly altered zones (e.g., Ehara Suryantini et al., 2005; Salama et al., 2025), the use of chlorite chemistry and SWIR-based vectoring is only applicable in areas where weathering is minimal and patchy.

Garnet chemistry at King also shows a distinction between footwall and hanging-wall stratigraphy. Garnet from hanging-wall units is characterized by significantly higher Ca contents compared to that from the footwall units (Fig. 8). This Ca enrichment in hanging-wall units has also been observed in VHMS deposits elsewhere (e.g., Wheatley deposit, Hassan, 2017; Stollberg ore field, Frank et al., 2019). It is likely that this Ca enrichment in the hanging-wall units is attributed to Ca-Mg carbonate alteration prior to metamorphism, which is the same signature we observed in white mica at King. In terms of trace elements, positive Eu anomalies in garnet are particularly useful to distinguish between altered footwall and unaltered hanging-wall units, thus retaining the signature of the host rock prior to metamorphism. Previous studies have suggested that positive Eu anomalies in whole-rock geochemical analyses in the proximity of massive sulfide mineralization are attributed to the lower oxygen fugacity (e.g., Lottermoser, 1988; Spry et al., 2007) and high-temperature hydrothermal fluids (e.g., Sverjensky, 1984). As demonstrated in this study, garnets from the footwall and massive sulfide lens consistently show prominent positive Eu anomalies, whereas this is less prominent or absent in the hanging-wall units (Fig. 10). Additionally, garnets from massive sulfides and the hanging wall are characterized by enrichments of Ba and Sr (Fig. 9E). The 11,100W feature in garnet is positively correlated with Ba + Sr ($r^2 = 0.7$), with these elements likely substituting for Mn^{2+} in the dodecahedral site (e.g., van Westrenen et al., 2000; Locock, 2008).

Garnet as a fertility indicator mineral in metamorphosed VHMS deposits?

Fertility indicator minerals have been extensively applied to several other ore deposit types, particularly for porphyry Cu-style mineralization using apatite (e.g., Mao et al., 2016), plagioclase (e.g., Williamson et al., 2016), zircon (e.g., Wilkinson et al., 2017), and magnetite (e.g., Sievwright, 2017). In VHMS systems, similar studies have been attempted using magnetite (e.g., Makvandi et al., 2016a, b), pyrite (e.g., Belousov et al., 2016; Li et al., 2024), and gahnite (e.g., Morris et al., 1997; O'Brien et al., 2015). Metamorphic minerals such as garnet potentially offer robust tools for assessing regional to camp-scale fertility for three reasons: (1) It occurs abundantly in high-grade metamorphic terranes; (2) it is the product of metamorphism, hence not affected either by recrystallization or metal remobilization; and (3) it is resistant to weathering in regolith profiles and can be preserved in stream sediments. As the VHMS host sequences will be hydrothermally altered prior to the metamorphism and porphyroblast growth, the garnet can preserve the hydrothermal signatures present in the altered host rock.

Garnet chemistry at King is dominated by the end-member almandine, which is typical for garnet in rocks subject to high-grade metamorphism (e.g., Yardley et al., 1991; Jamtveit et al., 1993; Crowe et al., 2001; Fernando et al., 2003). However, significant Mn enrichment (up to 22 wt % MnO) is observed in garnets hosted by the massive sulfide lens and the adjacent felsic footwall through EPMA. HyLogger TIR spectral shifts in garnet composition are dominated by shorter wavelength signatures (i.e., almandine; 11.25–11.45 µm) in the deep footwall. With stratigraphic height, there is a loss of these shorter wavelength signatures and a shift toward longer wavelength (i.e., more spessartine rich; 11.46–11.59 µm) compositions in the immediate footwall to massive sulfide mineralization (Fig. 2).

Similar Mn enrichment in almandine garnet spatially associated with massive sulfide mineralization has also been observed in VHMS deposits elsewhere (e.g., Yeats and Groves, 1998; Mercier-Langevin et al., 2007; Hassan, 2017; Hindemith et al., 2017; Frank et al., 2019; Praveen et al., 2021; Yergeau et al., 2022). A similar phenomenon was also observed in metamorphosed sedimentary exhalative (SEDEX) (e.g., Heimann et al., 2013; Pollock et al., 2018; Tott et al., 2019; Lisboa et al., 2023) and Broken Hill-type deposits (e.g., Spry and Wonder, 1989; Stalder and Rozendaal, 2005; Spry et al., 2007; Heimann et al., 2011). In contrast, almandine garnet from hanging-wall units at King shows significant enrichment in the grossular component ($Grs_{16–31}$; up to 11 wt % CaO).

Garnet compositions from several greenstone belts across Yilgarn craton have been compiled in Figure 8. Garnets from the Marda and Ravensthorpe greenstone belts are clustered with footwall garnet from King, in which VHMS mineralization has been reported from both of these greenstone belts (e.g., Marda-Copper Bore, Southern Gossan, Kim Bore, Ravensthorpe-Mount Short; Hollis et al., 2017). Several SEM-based studies have also reported significant Mn enrichment associated with massive sulfide mineralization in the Wheatley Zn deposit (at granulite facies; Hassan, 2017) and early, ca. 2930 Ma, synvolcanic VHMS mineralization at Mount Gibson that was later overprinted by ca. 2630 Ma orogenic Au mineralization (Yeats and Groves, 1998). In contrast, garnets from greenstone belts in which VHMS mineralization is absent (e.g., Forrestania, Laverton, Boorara, Coolgardie, Murin) are consistent with regional metamorphic garnet and hanging-wall signatures at King that lack an early synvolcanic hydrothermal signature.

Garnet trace element REE profiles also provide further discrimination for VHMS prospectivity. Under normal metamorphic conditions where the protolith is not hydrothermally altered, garnets from amphibolite and granulite facies rocks show typical metamorphic patterns of steep chondrite-normalized REE profiles (i.e., LREE depleted, absent of Eu anomaly, or negative Eu anomaly, dipping HREE profiles; e.g., Cruciani et al., 2014; Raimondo et al., 2017; Tual et al., 2022). In contrast, garnets from the footwall stratigraphy and massive sulfide

lens at King consistently show LREE depletion, positive Eu anomalies, and flat HREE patterns. Similar patterns have also been reported from several metamorphosed SEDEX and Broken Hill-type deposits (e.g., Spry et al., 2007; Heimann et al., 2011; Pollock et al., 2018; Tott et al., 2019; Lisboa et al., 2023) and from the Dammberget Pb-Ag-(Cu-Au) deposit, Sweden (Spry et al., 2015). The presence of positive Eu anomalies and HREE profiles in almandine garnet is particularly useful because these show a clear distinction between garnet spatially associated with mineralization and that from barren metamorphic rocks or igneous-origin almandine (Fig. 9B). Almandine garnet spatially associated with VHMS mineralization will be characterized by a positive Eu anomaly and has lower HREE (0.8–1,107 ppm) contents than garnet in regional metamorphic rocks (8.4–11,500 ppm). The REE patterns in garnet during metamorphism are influenced by several factors, including the bulk composition of the protolith, pressure-temperature (P-T) conditions, element partitioning among coexisting minerals, crystal chemistry, hydrothermal fluid activity, or a combination of these (e.g., Sverjensky, 1984; Bea et al., 1997; Moore et al., 2013). At the King deposit, metamorphism was limited to a single event (e.g., Goscombe et al., 2019), and the absence of correlations between garnet end members, REE concentrations, and Eu anomalies suggests that the effect of P-T conditions and crystal chemistry is minimal. The consistent positive Eu anomaly observed in footwall garnet, regardless of original protolith composition (i.e., mafic vs. felsic) or modal mineral assemblages, is best explained by feldspar destruction during premetamorphic hydrothermal alteration. This process is common during hydrothermal alteration within VHMS footwall but is rare or absent in the hanging-wall stratigraphy. Consequently, this process will release Eu^{2+} from feldspar, which was subsequently incorporated into the host lithology (e.g., Spry et al., 2007; Heimann et al., 2011). This also implies that the premetamorphic hydrothermal fluids were reducing in nature and of relatively high temperature (>250°C; Sverjensky, 1984; Heimann et al., 2011).

Several studies have used detrital garnet to understand its provenance (e.g., Andò et al., 2014; Krippner et al., 2014; Suggate and Hall, 2014), although the trace elements, including REEs, have not been evaluated. We propose that, due to its general resistance to weathering, garnet may serve as a fertility indicator mineral during regional prospecting (e.g., stream sediment or till sampling) in metamorphic terranes, as well as in shallow RC drilling campaigns through weathered saprock, though the latter requires further study. However, when garnet does weather, it undergoes significant loss of Si, Al, Ca, and Mg, while Mn is often leached or occasionally retained (Baidya et al., 2019). As garnet weathers to alumino-goethite, this then leads to a notable enrichment of LREEs, while the HREEs are largely inherited from the original garnet (Price et al., 2013; Baidya et al., 2019). Regarding garnet morphology, our study demonstrates that the texture of garnet (e.g., euhedral, skeletal, or heavily fractured and partially replaced) does not significantly affect its chemical signature. However, selecting inclusion-poor garnet with minimal zoning is ideal to minimize the potential for contamination during spot analysis in EPMA or LA-ICP-MS.

Application to prospects in the Erayinia region

The chemistry of chlorite, white mica, and garnet from the King deposit shows several potential chemical vectors to massive sulfide mineralization (Table 1). In this study, several rock-chip samples were also collected from regional prospects EB04 and EB16 to test the applicability of the mineral chemical vectors observed at King. Chlorite from the EB04 prospect was collected from the mafic and felsic footwall stratigraphy. RC drilling at the EB04 target stopped at the shallow depth of 150 m due to limitations of the drill rig to penetrate a late Proterozoic dolerite dike. The ore equivalent horizon was believed to have been tested by a narrow intercept of Zn mineralization (EC194: 8 m at 0.16% Zn; EC195: 6 m at 0.32% Cu, 0.12% Zn). At EB16, air core drilling intercepted bedrock at several locations to aid in geologic mapping and testing of soil anomalies.

At EB04, a similar pattern to King was observed, where the F and Mn contents in chlorite increase with depth toward the ore-equivalent horizon. Of note is that the F contents of chlorite and white mica from the EB04 felsic units are higher than those observed from the immediate felsic footwall at King. Chlorite from the Mg-metasomatized felsic unit at EB04 also has significantly higher Mg (median = 17 wt %) contents than that at King (median = 13 wt %). White mica chemistry further demonstrates that the sampled felsic rocks at EB04 prospect are still within the footwall due to its muscovitic composition and enrichment in Ba and Rb contents. As demonstrated at King, the hanging-wall stratigraphy is marked with phengitic white mica with Ba and Rb depletion. Petrographic analysis of rock chips confirmed that intercepted Zn mineralization at EB04 was of stringer style, typical of the felsic footwall. Addi-

Table 1. Summary of Mineral Chemical Vectors in the King Deposit and Surrounding Areas

Parameters	Characteristics
Proximity to ore (vertical)	Proximal signatures within 200 m: >0.3 wt % Mn in chlorite; >500 ppm F in chlorite and white mica; >5 ppm Tl in white mica; >30 mol % spessartine component in garnet
Mineralized versus barren system	Mineralized metamorphic belt: Total HREE <100 ppm; Eu anomaly >1 in garnet Barren metamorphic belt: Total HREE >100 ppm; Eu anomaly <1 in garnet
Footwall and hanging-wall distinction	Footwall signatures: Muscovitic white mica; Na muscovite in immediate FW; <50 ppm Sr, >250 ppm Ba, >50 ppm Rb in white mica; <15 mol % grossular component in garnet; >11 wt % Al in chlorite Hanging wall signatures: Phengitic white mica; >50 ppm Sr, <250 ppm Ba, <50 ppm Rb in white mica; >15 mol % grossular component in garnet; <11 wt % Al in chlorite
Protolith affinity	Mafic units: <0.1 Li/V in chlorite Felsic units: >0.1 Li/V in chlorite

Abbreviations: FW = footwall, HREE = heavy rare earth element

tionally, garnet chemistry at EB04 also shows footwall garnet signatures similar to garnet at King due to its slight enrichment in Mn (median = 5.6 wt % in felsic unit at EB04; 6.9 wt % in upper felsic unit at King) and lack of Ca enrichment (i.e., characteristic of hanging-wall garnet; median values of Ca at EB04 mafic-felsic units = 2.2 wt %; King footwall = 2.2 wt %; King hanging wall = 5.2 wt %). The REE pattern of garnets from the mafic and felsic units at EB04 further supports this interpretation, as it shows a pattern similar to garnet from the footwall units at King, although with a less prominent positive Eu anomaly (<3 Eu/Eu^*; Fig. 10). It is likely that the ore horizon is still concealed in the deeper part of the stratigraphy beneath the dolerite dike, and follow-up drilling is recommended to further test the target.

Samples from the EB16 prospect were collected only from the mafic rocks intercepted by air core drilling to evaluate whether the drilled region belongs to the footwall or hanging-wall stratigraphy (as garnet amphibolite can occur in both sequences). Samples were analyzed from the northern region presumed to be in the hanging wall and from the south in the footwall garnet amphibolite (Fig. 1D). In this instance, chlorite chemistry is not particularly useful, as it is unable to distinguish between footwall and hanging-wall units. However, chlorite from EB16 mafic units is slightly more enriched in F than that from mafic footwall or hanging wall at King. Garnet from the EB16 mafic units also plots with the same cluster with footwall garnets from King and EB04 and lacks the Ca enrichment of hanging-wall rocks. This suggests that the mafic units at EB16 from both areas sampled most likely belong to the footwall sequence, and further drilling should target the felsic rocks higher in the stratigraphy.

Conclusions

The compositions of chlorite, white mica, and garnet, coupled with hyperspectral data, can be used as robust vectoring tools in the search for metamorphosed VHMS deposits. This includes utilizing fluorine in chlorite and white mica, as well as manganese in chlorite and garnet, to trace hydrothermal alteration surrounding metamorphosed VHMS deposits. Various elements in chlorite, white mica, and garnet also help differentiate between the footwall and hanging-wall stratigraphy of VHMS deposits in metamorphic terranes, and the original protolith affinity (i.e., mafic vs. felsic). Additionally, positive Eu anomalies and dipping HREE profiles in almandine garnet effectively distinguish garnet spatially associated with VHMS mineralization from that derived from barren metamorphic rocks or igneous-origin almandine. The geochemical signatures defined here are not only useful for deposit-scale exploration but also for regional prospecting, such as stream sediment or till sampling in metamorphic terranes, as well as for shallow RC/air core drilling through weathered saprolite and saprock.

Author Contributions

1. C.D.P.D.: Conceptualization, investigation, methodology, formal analysis, visualization, writing—original draft.
2. S.P.H.: Conceptualization, investigation, methodology, writing—review editing, funding acquisition, supervision.
3. P.G.S.: Conceptualization, interpretation, validation, resources, writing—review editing.
4. C.J.R.: Investigation, methodology, formal analysis, writing—review editing.
5. M.J.: Investigation, writing—review editing, resources, supervision, funding acquisition.
6. D.P.: Investigation, writing—review editing, resources, supervision, funding acquisition, project administration.
7. R.A.: Investigation, resources, writing—review editing.

Declaration of Competing Interests

M.J., D.P., and R.A. are either employees of Black Raven Mining or have undertaken contract work for Black Raven Mining. The paper reflects the views of the scientists and not the company.

Acknowledgments

This study is funded by a National Environment Research Council Doctoral Training Partnership grant (NE/S007407/1). Drilling by Black Raven Mining at EB04 was co-funded through the Exploration Incentive Scheme of Western Australia state government. Ivan Febbrari is thanked for preparing the polished thin sections used in this study. Laetitia Pichevin and Chris Hayward are thanked for technical assistance during LA-ICP-MS and EPMA, respectively. Samples used in this study from hole EC116D were made available by the Geological Survey of Western Australia. Insightful comments and suggestions from the reviewers, Paul Duuring and Derek Leung, and Associate Editor Stefanie Brueckner are greatly appreciated.

Data Availability Statement

New data generated during this research are contained within the article and supplementary materials. Restrictions apply to the availability of the company drilling database.

REFERENCES

Aiuppa, A., Baker, D.R., and Webster, J.D., 2009, Halogens in volcanic systems: Chemical Geology, v. 263, p. 1–8, https://doi.org/10.1016/j.chemgeo.2008.10.005.

Andò, S., Morton, A., and Garzanti, E., 2014, Metamorphic grade of source rocks revealed by chemical fingerprints of detrital amphibole and garnet: Geological Society Special Publication, v. 386, p. 351–371, https://doi.org/10.1144/SP386.

Baidya, A.S., Pal, D.C., and Upadhyay, D., 2019, Chemical weathering of garnet in banded iron formation: Implications for the mechanism and sequence of secondary mineral formation and mobility of elements: Geochimica et Cosmochimica Acta, v. 265, p. 198–220, https://doi.org/10.1016/j.gca.2019.08.0370016-7037.

Barrote, V.R., Tessalina, S.G., McNaughton, N.J., Evans, N.J., Hollis, S.P., and McDonald, B.J., 2020, Surge of ore metals in seawater and increased bio-activity: A tracer of VHMS mineralization in Archaean successions, Yilgarn craton, Western Australia: Mineralium Deposita, v. 56, p. 643–664, https://doi.org/10.1007/s00126-020-00986-6.

Bea, F., Montero, P., Garuti G., and Zacharini, F., 1997, Pressure-dependence of rare earth element distribution in amphibolite- and granulite-grade garnets: A LA-ICP-MS study: Geostandards Newsletter, v. 21, p. 253–270, https://doi.org/10.1111/j.1751-908X.1997.tb00674.x.

Belford, S., 2010, Genetic and chemical characterisation of the host succession to the Archean Jaguar VHMS deposit: Unpublished PhD thesis, Hobart, Australia, University of Tasmania, 392 p.

Belousov, I., Large, R.R., Meffre, S., Danyushevky, L.V., Steadman, J., and Beardsmore, T., 2016, Pyrite compositions from VHMS and orogenic Au deposits in the Yilgarn craton, Western Australia: Implications for gold and copper exploration: Ore Geology Reviews, v. 79, p. 474–499, https://doi.org/10.1016/j.oregeorev.2016.04.020.

Cai, D., Shao, H., Gou, L.-F., Jin, Z., and Yang, S., 2024, Lithium isotope fractionation during submarine hydrothermal alteration

processes: Geochimica et Cosmochimica Acta, v. 371, p. 65–77, https://doi.org/10.1016/j.gca.2024.03.005.
Carroll, M.R., and Webster, J.D., 1994, Solubilities of sulfur, noble gases, nitrogen, chlorine, and fluorine in magmas: Reviews in Mineralogy and Geochemistry, v. 30, p. 231–279.
Cassidy, K.F., Champion, D.C., Krapez, B., et al., 2006, A revised geological framework for the Yilgarn craton, Western Australia: Western Australia Geological Survey, Record 2006/8, 8 p.
Cloutier, J., Piercey, J., and Hutington, J., 2021, Mineralogy, mineral chemistry and SWIR spectral reflectance of chlorite and white mica: Minerals, v. 11, article 471, https://doi.org/10.3390/min11050471.
Cravinho, A., Rosa, D., Relvas, J.M.R.S., et al., 2024, From source to surface: Clues from garnet-bearing Carboniferous silicic volcanic rocks, Iberian Pyrite Belt, Portugal: Contributions to Mineralogy and Petrology, v. 179, no. 32, https://doi.org/10.1007/s00410-024-02106-3.
Crowe, D.E., Riciputi, L.R., Bezenek, S., and Ignatiev, A., 2001, Oxygen isotope and trace element zoning in hydrothermal garnets: Windows into large-scale fluid flow behavior: Geology, v. 29, p. 479–482, https://doi.org/10.1130/0091–7613(2001)029<0479:OIATEZ>2.0.CO;2.
Cruciani, G., Franceschelli, M., Foley, S.F., and Jacob, D.E., 2014, Anatectic amphibole and restitic garnet in some Variscan migmatite from NE Sardinia, Italy: Insights into partial melting from mineral trace elements: European Journal of Mineralogy, v. 26, p. 381–395, https://doi.org/10.1127/0935-1221/2014/0026-2376.
Czarnota, K., Champion, D.C., Goscombe, B., et al., 2010, Geodynamics of the eastern Yilgarn craton: Precambrian Research, v. 183, p. 175–202, https://doi.org/10.1016/j.precamres.2010.08.004.
Dana, C.D.P., Hollis, S.P., Podmore, D., James, M., and Azri, R., 2025, Using coupled bulk-rock geochemistry and short-wave infrared (SWIR) spectral reflectance data as rapid exploration tools in metamorphosed VHMS deposits: Insights from the King Zn deposit, Yilgarn craton, Western Australia: Mineralium Deposita, v. 60, p. 1117–1140, https://doi.org/10.1007/s00126-024-01342-8.
DeVries, R.C., and Roy, R., 1958, The influence of ionic substitution on the stability of micas and chlorites: Economic Geology, v. 53, p. 958–965, https://doi.org/10.2113/gsecongeo.53.8.958.
Drummond, D.A., Cloutier, J., Boyce, A.J., and Prave, A.R., 2020, Petrogenesis and geochemical halos of the amphibolite facies, Lower Proterozoic, Kerry Road volcanogenic massive sulfide deposit, Loch Maree Group, Gairloch, NW Scotland: Ore Geology Reviews, v. 124, article 103623, https://doi.org/10.1016/j.oregeorev.2020.103623.
Dusel-Bacon, C., 2012, Petrology of metamorphic rocks associated with volcanogenic massive sulfide deposits: U.S. Geological Survey Scientific Investigations Report, 2010-5070-C, 345 p.
Dutrow, B.L., Holdaway, M.J., and Hinton, R.W., 1986, Lithium in staurolite and its petrologic significance: Contributions to Mineralogy and Petrology, v. 94, p. 496–506, https://doi.org/10.1007/BF00376341.
Duuring, P., Hassan, L., Zelic, M., and Gessner, K., 2016, Geochemical and spectral footprint of metamorphosed and deformed VMS-style mineralization in the Quinns district, Yilgarn craton, Western Australia: Economic Geology, v. 111, p. 1411–1438, https://doi.org/10.2113/econgeo.111.6.1411.
Edmond, J.M., Measures, C., McDuff, R.E., Chan, L.H., Collier, R., and Grant, B., 1979, Ridge crest hydrothermal activity and the balances of the major and minor elements in the ocean: The Galapagos data: Earth and Planetary Science Letters, v. 46, p. 1–18, https://doi.org/10.1016/0012-821X(79)90061-X.
Ehara Suryantini, S., van Ruitenbeek, F.J., and van der Meer, F.D., 2005, The effect of weathering on reflectance spectra of hydrothermal white micas and chlorites: Implications for alteration mapping, *in* Mao, J., Bierlein, F.P., eds., Mineral deposit research: Meeting the global challenge: Springer, https://doi.org/10.1007/3-540-27946-6_179.
Fernando, G.W.A.R., Hauzenberger, C.A., Baumgartner, L.P., and Hofmeister, W., 2003, Modelling of retrograde diffusion zoning in garnet: Evidence for slow cooling of granulites from the Highland Complex of Sri Lanka: Mineralogy and Petrology, v. 78, p. 53–71, https://doi.org/10.1007/s00710–002–0224–1.
Frank, K.S., Spry, P.G., Raat, H., Allen, R., Jansson, N.F., and Ripa, M., 2019, Variability in the geologic, mineralogical, and gochemical characteristics of base metal sulfide deposits in the Stollberg ore field, Bergslagen district, Sweden: Economic Geology, v. 114, p. 473–511, https://doi.org/10.5382/econgeo.4646.
Franklin, J.M., Gibson, H.L., Jonasson, I.R., and Galley, A.G., 2005, Volcanogenic massive sulfide deposits: Economic Geology 100th Anniversary Volume, p. 525–560, https://doi.org/10.5382/AV100.17.
Galley, A.G., 1993, Characteristics of semi-conformable alteration zones associated with volcanogenic massive sulphide districts: Journal of Geochemical Exploration, v. 48, p. 175–200, https://doi.org/10.1016/0375-6742(93)90004-6.
Gibson, H.L., Allen, R.L., Riverin, G., and Lane, T.E., 2007, The VMS model: Advances and application to exploration targeting: Exploration 07: Fifth Decennial International Conference on Mineral Exploration, Toronto, Canada, September 9–12, 2007, p. 713–730.
Gieskes, J.M., Simoneit, B.R.T., Goodfellow, W.D., Baker, P.A., and Mahn, C., 2002, Hydrothermal geochemistry of sediments and pore waters in Escanaba Trough—ODP Leg 169: Applied Geochemistry, v. 17, p. 1435–1456, https://doi.org/10.1016/S0883-2927(02)00111-7.
Gisbert, G., Tornos, F., Losantos, E., et al., 2022, Vectors to ore in replacive volcanogenic massive sulphide deposits of the northern Iberian Pyrite Belt: Major and trace element mineral chemistry: Ore Geology Reviews, v. 147, article 104963, https://doi.org/10.1016/j.oregeorev.2022.104963.
Goscombe, B.D., Blewett, R.S., Czarnota, K., Groenewwald, B.A., and Maas, R., 2009, Metamorphic evolution and integrated terrane analysis of the eastern Yilgarn craton: Rationale, methods, outcomes and interpretation: Geoscience Australia, Record 2009/23, https://pid.geoscience.gov.au/dataset/ga/68806.
Goscombe, B.D., Foster, D.A., Blewett, R., et al., 2019, Neoarchaean metamorphic evolution of the Yilgarn craton: A record of subduction, accretion, extension and lithospheric delamination: Precambrian Research, v. 335, article 105441, https://doi.org/10.1016/j.precamres.2019.105441.
Guilliamse, J., 2014, Assessing the potential for volcanic-associated massive sulfide mineralization at Weld Range, using Golden Grove for comparison: Geological Survey of Western Australia, Report 141, 61 p.
Halley, S.W., Wood, D., Stoltze, A., Godfroid, J., Goswell, H., and Jack, D., 2016, Using multielement geochemistry to map multiple components of a mineral system: Case study from a sediment-hosted Cu-Ni camp, NW Province, Zambia: SEG Discovery, v. 104, p. 1–21, https://doi.org/10.5382/SEGnews.2016-104.fea.
Hammerli, J., and Rubenach, M., 2018, The role of halogens during regional and contact metamorphism, *in* Harlov, D.E., and Aranovich, L., eds., The role of halogens in terrestrial and extraterrestrial geochemical processes: Surface, crust, and mantle: Springer, p. 649–712.
Hammerli, J., Spandler, C., Oliver, N.H.S., and Rusk, B., 2014, Cl/Br of scapolite as a fluid tracer in the earth's crust: Insights into fluid sources in the Mary Kathleen fold belt, Mt. Isa inlier, Australia: Journal of Metamorphic Geology, v. 32, p. 93–112.
Hancock, E.A., Green, A.A., Huntington, J.F., Schodlok, M.C., and Whitbourne, L.B., 2013, HyLogger-3: Implication of adding thermal-infrared sensing: Geological Survey of Western Australia, Record 2013/3, 24 p.
Hannington, M.D., 2014, Volcanogenic massive sulfide deposits, *in* Holland, H.D., and Turekian, K.K., eds., Treatise on Geochemistry, 2nd edition: Elsevier, p. 463–488, https://doi.org/10.1016/B978-0-08-095975-7.01120-7.
Hannington, M.D., Kjarsgaard, I.M., Galley, A.G., and Taylor, B., 2003, Mineral-chemical studies of metamorphosed hydrothermal alteration in the Kristineberg volcanogenic massive sulfide district, Sweden: Mineralium Deposita, vol. 38, p. 423–442, https://doi.org/10.1007/s00126-002-0299-y.
Hassan, L.Y., 2014, The Yuinmery volcanogenic massive sulfide prospects: Mineralization, metasomatism and geology: Geological Survey of Western Australia, Report 131, 65 p.
Hassan, L.Y., 2017, Alteration associated with the Austin-Quinns VMS prospects, northern Yilgarn craton: Geological Survey of Western Australia, Record 2017/10, 61 p.
Hayman, P.C., Hull, S.E., Cas, R.A.F., et al., 2015, A new period of volcanogenic massive sulfide formation in the Yilgarn: A volcanological study of the ca. 2.76 Ga Hollandaire VMS deposit, Yilgarn craton, Western Australia: Australian Journal of Earth Sciences, v. 62, p. 189–210, https://doi.org/10.1080/08120099.2015.1011399.
Heimann, A., Spry, P.G., Teale, G.S., Conor, C.H.H., and Pearson, N.J., 2005, Major and rare-earth element chemistry of garnet-rich rocks in the Curnamona Province, Australia: Implications for Broken Hill-type mineralization [abs.]: Geological Society of America Abstracts with Programs, v. 37, no. 7, p. 452.
Heimann, A., Spry, P.G., Teale, G.S., Conor, C.H.H., and Leyh, W.R., 2009, Geochemistry of garnet-rich rocks in the southern Curnamona Province, Australia, and their genetic relationship to Broken Hill-type Pb-Zn-Ag mineralization: Economic Geology, v. 104, p. 687–712, https://doi.org/10.2113/gsecongeo.104.5.687.
Heimann, A., Spry, P.G., Teale, G.S., Conor, C.H.H., and Leyh, W.R., 2011, The composition of garnet in garnet-rich rocks in the southern Proterozoic

Curnamona Province, Australia: An indicator of the premetamorphic physicochemical conditions of formation: Mineralogy and Petrology, v. 101, p. 49–74, https://doi.org/10.1007/s00710-010-0130-x.

Heimann, A., Spry, P.G., Teale, G.S., et al., 2013, Geochemistry and genesis of low-grade metasediment-hosted Zn-Pb-Ag mineralization, southern Proterozoic Curnamona Province, Australia: Journal of Geochemical Exploration, v. 128, p. 97–116, https://doi.org/10.1016/j.gexplo.2013.02.007.

Hindemith, M., Indares, A., and Piercey, S., 2017, Hydrothermally altered volcanic rocks metamorphosed at granulite-facies conditions: An example from the Grenville Province: Canadian Journal of Earth Sciences, v. 54, p. 622–638, https://doi.org/10.1139/cjes-2016-0146.

Hollis, S.P., Yeats, C.J., Wyche, S., et al., 2015, A review of volcanic-hosted massive sulphide (VHMS) mineralization in the Archaean Yilgarn craton, Western Australia: Tectonic, stratigraphic and geochemical associations: Precambrian Research, v. 260, p. 113–135, https://doi.org/10.1016/j.precamres.2014.11.002.

Hollis, S.P., Mole, D.R., Gillespie, P., et al., 2017, 2.7 Ga plume associated VHMS mineralization in the Eastern Goldfields superterrane, Yilgarn craton: Insights from the low temperature and shallow water, Ag-Zn-(Au) Nimbus deposit: Precambrian Research, v. 291, p. 119–142, https://doi.org/10.1016/j.precamres.2017.01.002.

Hollis, S.P., Podmore, D., James, M., Kneeshaw, A., and Beaton, R., 2019a, Targeting VHMS mineralization at Erayinia in the Eastern Goldfields superterrane using lithogeochemistry, soil chemistry and HyLogger data: Journal of Geochemical Exploration, v. 207, article 106379, https://doi.org/10.1016/j.gexplo.2019.106379.

Hollis, S.P., Podmore, D., James, M., et al., 2019b, VHMS mineralisation at Erayinia in the Eastern Goldfields superterrane: Geology and geochemistry of the metamorphosed King Zn deposit: Australian Journal of Earth Sciences, v. 66, p. 153–181, https://doi.org/10.1080/08120099.2018.1515577.

Hollis, S.P., Foury, S., Caruso, S., Johnson, S., Barrote, V., and Pumphrey, A., 2021, Lithogeochemical and hyperspectral halos to Ag-Zn-Au mineralization at Nimbus in the Eastern Goldfields superterrane, Western Australia: Minerals, v. 11, article 254, https://doi.org/10.3390/min11030254.

Huston, D.L., Champion, D.C., and Cassidy, K.F., 2014, Tectonic controls on the endowment of Neoarchean cratons in volcanic-hosted massive sulfide deposits: Evidence from lead and neodymium isotopes: Economic Geology, v. 109, p. 11–26, https://doi.org/10.2113/econgeo.109.1.11.

Ivanic, T.J., Wingate, M.T.D., Kirkland, C.L., van Kranendonk, M.J., and Wyche, S., 2010, Age and significance of voluminous mafic-ultramafic magmatic events in the Murchison domain, Yilgarn craton: Australian Journal of Earth Sciences, v. 57, p. 597–614, https://doi.org/10.1080/08120099.2010.494765.

Izawa, M.R.M., Cloutis, E.A., Rhind, T., et al., 2018, Spectral reflectance (0.35–2.5 μm) properties of garnets: Implications for remote sensing detection and characterization: Icarus, v. 300, p. 392–410, https://doi.org/10.1016/j.icarus.2017.09.005.

James, R.H., Green, D.R.H., Stock, M.J., et al., 2014, Composition of hydrothermal fluids and mineralogy of associated chimney material on the East Scotia Ridge back-arc spreading centre: Geochimica et Cosmochimica Acta, v. 139, p. 47–71, https://doi.org/10.1016/j.gca.2014.04.024.

Jamtveit, B., Wogelius, R.A., and Fraser, D.G., 1993, Zonation patterns of skarn garnets: Records of hydrothermal system evolution: Geology, v. 21, p. 113–116, https://doi.org/10.1130/0091–7613(1993)021<0113:ZPOSGR>2.3.CO;2.

Jochum, K.P., Nohl, U., Herwig, K., Lammel, E., Stoll, B., and Hofmann, A.W., 2005, GeoReM: A new geochemical database for reference materials and isotopic standards: Geostandards and Geoanalytical Research, v. 29, p. 333–338, https://doi.org/10.1111/j.1751-908X.2005.tb00904.x.

Jones, S.A., 2007, Geology of the Erayinia 1:100,000 sheet: Western Australia Geological Survey, 1:100,000 Geological Series Explanatory Notes, 37 p.

Jowitt, S.M., Jenkin, G.R.T., Coogan, L.A., and Naden, J., 2012, Quantifying the release of base metals from source rocks for volcanogenic massive sulfide deposits: Effects of protolith composition and alteration mineralogy: Journal of Geochemical Exploration, v. 112, p. 47–59, https://doi.org/10.1016/j.gexplo.2012.04.005.

Kelly, J., Hollis, S.P., Dana, C.D.P., Kneeshaw, A., Podmore, D., and James, M., 2024, Characterization of a metamorphosed volcanic stratigraphy and VMS alteration halos using rock chip petrography and lithogeochemistry: A case study from King North, Yilgarn craton, Western Australia: Minerals, v. 14, no. 5, article 481, https://doi.org/10.3390/min14050481.

Kendrick, M., 2018, Halogens in seawater, marine sediments, and the altered oceanic lithosphere, *in* Harlov, D.E., and Aranovich, L., eds., The role of halogens in terrestrial and extraterrestrial geochemical processes: Surface, crust, and mantle: Springer, p. 591–648.

Kimberley, M.M., 1989, Exhalative origins of iron formations: Ore Geology Reviews, v. 5, p. 13–145, https://doi.org/10.1016/0169-1368(89)90003-6.

Koopman, E.R., Hannington, M.D., Santaguida, F., and Cameron, B.I., 1999, Petrology and geochemistry of proximal hydrothermal alteration in the Miner Rhyolite at Kidd Creek: Economic Geology Monograph, v. 10, p. 267–296.

Krippner, A., Meinhold, G., Morton, A.C., and von Eynatten, H., 2014, Evaluation of garnet discrimination diagrams using geochemical data of garnets derived from various host rocks: Sedimentary Geology, v. 306, p. 36–52, https://doi.org/10.1016/j.sedgeo.2014.03.004.

Laakso, K., Peter, J.M., Rivard, B., and White, H.P., 2016, Short-wave infrared spectral and geochemical characteristics of hydrothermal alteration at the Archean Izok Lake Zn-Cu-Pb-Ag volcanogenic massive sulfide deposit, Nunavut, Canada: Application in exploration target vectoring: Economic Geology, v. 111, p. 1223–1239, https://doi.org/10.2113/econgeo.111.5.1223.

Large, R.R., Gemmell, J.B., Paulick, H., and Huston, D.L., 2001, The alteration box plot: A simple approach to understanding the relationship between alteration mineralogy and lithogeochemistry associated with volcanic-hosted massive sulfide deposits: Economic Geology, v. 96, p. 957–971, https://doi.org/10.2113/gsecongeo.96.5.957.

Laukamp, C., Rodger, A., LeGras, M., et al., 2021, Mineral physicochemistry underlying feature-based extraction of mineral abundance and composition from shortwave, mid and thermal infrared reflectance spectra: Minerals, v. 11, article 347, https://doi.org/10.3390/min11040347.

Lavery, N.G., 1985, The use of fluorine as a pathfinder for volcanic-hosted massive sulfide ore deposits: Journal of Geochemical Exploration, v. 23, p. 35–60, https://doi.org/10.1016/0375-6742(85)90015-9.

Li, H., Zhang, Z., Zhang, R., et al., 2024, Geochemical discrimination of pyrite in diverse ore deposit types through statistical analysis and machine learning techniques: American Mineralogist, v. 109, p. 846–857, https://doi.org/10.2138/am-2023-8976.

Lisboa, L.H.D., Filho, C.F.F., Monteiro, L.V.S., and Mansur, E.T., 2023, Gahnite, garnet and magnetite compositions of metamorphosed sediment-hosted Zn-Pb-(Cu-Ag) deposits of the Mesoproterozoic Nova Brasilândia Group: Vectors for SEDEX deposits with Broken Hill-type affinities in the western Amazonian craton, Brazil: Journal of Geochemical Exploration, v. 249, article 107210, https://doi.org/10.1016/j.gexplo.2023.107210.

Locock, A.J., 2008, An Excel spreadsheet to recast analyses of garnet into end-member components, and a synopsis of the crystal chemistry of natural silicate garnets: Computers and Geosciences, v. 34912, p. 1769–1780, https://doi.org/10.1016/j.cageo.2007.12.013.

Lottermoser, B.G., 1988, Rare earth element composition of garnets from the Broken Hill Pb-Zn-Ag orebodies, Australia: Neues Jahrbuch fur Mineralogie Montatshefte, v. 9, p. 423–431.

Lucci, F., Rossetti, F., Becchio, R., et al., 2018, Magmatic Mn-rich garnets in volcanic settings: Age and longevity of the magmatic plumbing system of the Miocene Ramadas volcanism (NW Argentina): Lithos, v. 322, p. 238–249, https://doi.org/10.1016/j.lithos.2018.10.016.

Makvandi, S., Ghasemzadeh-Barvarz, M., Beaudoin, G., Grunsky, E.C., McClenaghan, M.B., and Duchesne, C., 2016a, Principal component analysis of magnetite composition from volcanogenic massive sulfide deposits: Case studies from the Izok Lake (Nunavut, Canada) and Halfmile Lake (New Brunswick, Canada) deposits: Ore Geology Reviews, v. 72, p. 60–85, https://doi.org/10.1016/j.oregeorev.2015.06.023.

Makvandi, S., Ghasemzadeh-Barvarz, M., Beaudoin, G., et al. 2016b, Partial least squares-discriminant analysis of trace element compositions of magnetite from various VMS deposit subtypes: Application to mineral exploration: Ore Geology Reviews, v. 78, p. 388–408, https://doi.org/10.1016/j.oregeorev.2016.04.014.

Mao, M., Rukhlov, A.S., Rowins, S.M., Spence, J., and Coogan, L.A., 2016, Apatite trace element compositions: A robust new tool for mineral exploration: Economic Geology, v. 111, p. 1187–1222, https://doi.org/10.2113/econgeo.111.5.1187.

Markl, G., Musashi, M., and Bucher, K., 1997, Chlorine stable isotope composition of granulites from Lofoten, Norway: Implications for the Cl isotopic composition and for the source of Cl enrichment in the lower crust: Earth and Planetary Science Letters, v. 150, p. 95–102, https://doi.org/10.1016/S0012-821X(97)00084-8.

McDonough, W.F., and Sun, S.S., 1995, Composition of the earth: Chemical Geology, v. 120, p. 223–253, https://doi.org/10.1016/0009-2541(94)00140-4.

Mercier-Langevin, P., Dubé, B., Hannington, M.D., Richer-Laflèche, M., and Gosselin, G., 2007, The LaRonde Penna Au-rich volcanogenic massive sulfide deposit, Abitibi greenstone belt, Quebec: Part II. Lithogeochemistry

and paleotectonic setting: Economic Geology, v. 102, p. 611–631, https://doi.org/10.2113/gsecongeo.102.4.611.

Mole, D.R., Fiorentini, M.L., Cassidy, K.F., et al., 2014, Crustal evolution, intra-cratonic architecture and the metallogeny of an Archaean craton: Geological Society Special Publication, v. 393, p. 23–80, https://doi.org/10.1144/SP393.8.

Moore, S.J., Carlson, W.D., and Hesse, M.A., 2013, Origins of yttrium and rare earth element distributions in metamorphic garnet: Journal of Metamorphic Geology, v. 31, p. 663–689, https://doi.org/10.1111/jmg.12039.

Morris, T.F., Breaks, F.W., Averill, S.A., Crabtree, D.C., and McDonald, A., 1997, Gahnite composition: Implication for base metal and rare-element exploration: Exploration and Mining Geology, v. 6, p. 253–260.

Munoz, J.L., 1984, F-OH and Cl-OH exchange in micas with applications to hydrothermal ore deposits: Reviews in Mineralogy and Geochemistry, v. 13, p. 469–493.

Nesbitt, B.E., 1982, Metamorphic sulfide-silicate equilibria in the massive sulfide deposits at Ducktown, Tennessee: Economic Geology, v. 77, p. 364–378, https://doi.org/10.2113/gsecongeo.77.2.364.

O'Brien, J.J., Spry, P.G., Teale, G.S., Jackson, S.E., and Koenig, A.E., 2015, Gahnite composition as a means to fingerprint metamorphosed massive sulfide and non-sulfide zinc deposits: Journal of Geochemical Exploration, v. 159, p. 48–61, https://doi.org/10.1016/j.gexplo.2015.08.005.

Osei, K.P., Kirkland, C.L., and Mole, D.R., 2021, Nd and Hf isoscapes of the Yilgarn craton, Western Australia and implications for its mineral systems: Gondwana Research, v. 92, p. 253–265, https://doi.org/10.1016/j.gr.2020.12.027.

Perfit, M.R., Ridley, W.I., and Jonasson, I.R., 1997, Geologic, petrologic and geochemical relationships between magmatism and massive sulfide mineralization along the eastern Galapagos spreading center: Reviews in Economic Geology, v. 8, p. 75–100, https://doi.org/10.5382/Rev.08.

Plimer, I.R., 2006, Manganoan garnet rocks associated with the Broken Hill Pb-Zn-Ag orebody, Australia: Mineralogy and Petrology, v. 86, p. 443–478.

Pollock, M.V., Spry, P.G., Tott, K.A., Koenig, A., Both, R.A., and Ogierman, J., 2018, The origin of the sediment-hosted Kanmantoo Cu-Au deposit, South Australia: Mineralogical considerations: Ore Geology Reviews, v. 95, p. 94–117, https://doi.org/10.1016/j.oregeorev.2018.02.017.

Praveen, M.N., Nambiar, C.G., and Huston, D.L., 2021, Geochemistry and petrogenesis of Paleoproterozoic rhyolite-hosted zinc-rich metamorphosed volcanogenic massive sulfide deposits in the eastern Betul belt, central India: Ore Geology Reviews, v. 13, article 103918, https://doi.org/10.1016/j.oregeorev.2020.103918.

Price, J.R., Bryan-Ricketts, D.S., Anderson, D., and Velbel, M.A., 2013, Weathering of almandine garnet: Influence of secondary minerals on the rate-determining step, and implications for regolith-scale Al mobilization: Clays and Clay Minerals, v. 61, p. 34–56, https://doi.org/10.1346/CCMN.2013.0610104.

Quinby-Hunt, M.S., and Turehian, K.K., 1983, Distribution of elements in sea water: Eos, Transactions American Geophysical Union, v. 64, p. 129–132, https://doi.org/10.1029/EO064i014p00130.

Raimondo, T., Payne, J., Wade, B., Lanari, P., Clark, C., and Hand, M., 2017, Trace element mapping by LA-ICP-MS: Assessing geochemical mobility in garnet: Contributions to Mineralogy and Petrology, v. 172, no. 17, https://doi.org/10.1007/s00410-017-1339-z.

Reeves, E.P., Seewald, J.S., Saccocia, P., et al., 2011, Geochemistry of hydrothermal fluids from the PACMANUS, northeast Pual and Vienna Woods hydrothermal fields, Manus basin, Papua New Guinea: Geochimica et Cosmochimica Acta, v. 75, p. 1088–1123, https://doi.org/10.1016/j.gca.2010.11.008.

Reyes, A.G., and Trompetter, W.J., 2012, Hydrothermal water-rock interaction and the redistribution of Li, B and Cl in the Taupo volcanic zone, New Zealand: Chemical Geology, v. 314–317, p. 96–112, https://doi.org/10.1016/j.chemgeo.2012.05.002.

Salama, W., Goswami, N., Lampinen, H., Verrall, M., and Schnoveld, L., 2025, Mapping hydrothermal alteration in regolith using white micas and chlorite as vectors towards gold mineralization: Journal of Geochemcial Exploration, v. 268, article 107603, https://doi.org/10.1016/j.gexplo.2024.107603.

Schumacher, J.C., 1991, Empirical ferric iron corrections: Necessity, assumptions, and effects on selected geothermobarometers: Mineralogical Magazine, v. 55, p. 1493–1504, https://doi.org/10.1180/minmag.1991.055.378.02.

Selverstone, J., and Sharp, Z.D., 2015, Chlorine isotope behavior during prograde metamorphism of sedimentary rocks: Earth and Planetary Science Letters, v. 417, p. 120–131, https://doi.org.10.1016/j.epsl.2015.02.030.

Seyfried, W.E., and Ding, K., 1995, The hydrothermal chemistry of fluoride in seawater: Geochimica et Cosmochimica Acta, v. 59, p. 1063–1071, https://doi.org/10.1016/0016-7037(95)00023-S.

Sharpe, R., 1999, The Archean Cu-Zn magnetite-rich Gossan Hill VHMS deposit, Western Australia: Evidence of a structurally-focused, exhalative and sub-seafloor replacement mineralizing system: PhD thesis, University of Tasmania.

Sharpe, R., and Gemmell, J.B., 2002, The Archean Cu-Zn magnetite-rich Gossan Hill volcanic-hosted massive sulfide deposit, Western Australia: Genesis of a multistage hydrothermal system: Economic Geology, v. 97, p. 517–539, https://doi.org/10.2113/gsecongeo.97.3.517.

Sievwright, R., 2017, Developing magnetite chemistry as an exploration tool for porphyry copper deposits: Unpublished PhD thesis, Imperial College, London, 340 p.

Soltani Dehnavi, A., Lentz, D.R., McFarlane, C.R.M., and Walker, J.A., 2018, Quantification of fluid-mobile elements in white mica by LA-ICP-MS: From chemical composition to a potential micro-chemical vectoring tool in VMS exploration: Journal of Geochemical Exploration, v. 188, p. 290–307, https://doi.org/10.1016/j.gexplo.2018.01.017.

Soltani Dehnavi, A., McFarlane, C.R.M., Lentz, D.R., McClenaghan, S.H., and Walker, J.A., 2019, Chlorite-white mica pairs' composition as a microchemical guide to fingerprint massive sulfide deposits of the Bathurst mining camp, Canada: Minerals, v. 9, article 125, https://doi.org/10.3390/min9020125.

Spry, P.G., 1998, Sulfidation and oxidation haloes as guides in the exploration for metamorphosed massive sulfide ores: Reviews in Economic Geology, v. 11, p. 153–165, https://doi.org/10.5382/Rev.11.07.

Spry, P.G., and Wonder, J.D., 1989, Manganese-rich garnet rocks associated with the Borken Hill lead-zinc-silver deposit, New South Wales, Australia: Canadian Mineralogist, v. 27, p. 275–292.

Spry, P.G., Heimann, A., Messerly, J.D., and Houk, R.S., 2007, Discrimination of metamorphic and metasomatic processes at the Broken Hill Pb-Zn-Ag deposit, Australia: Rare earth element signatures of garnet-rich rocks: Economic Geology, v. 102, p. 471–494, https://doi.org/10.2113/gsecongeo.102.3.471.

Spry, P.G., O'Brien, J.J., Frank, K.S., et al., 2015, Trace element compositions of silicates and oxides as exploration guides to metamorphosed massive sulphide deposits: Examples from Broken Hill, Australia, and Stollberg, Sweden: 27th International Applied Geochemistry Symposium: Application of Indicator Mineral Methods to Mineral Exploration, Short Course SCO2, Association of Applied Geochemistry, April 20–24, 2015, Tucson, Arizona, USA, p. 7.

Spry, P.G., Berke, E.H., Layton-Matthews, D., et al., 2024, The trace-element compositions of amphibole, magnetite and ilmenite as potential exploration guides to metamorphosed Proterozoic Cu-Zn ± Pb ± Au ± Ag volcanogenic massive sulfide deposits in Colorado, USA: Mineralogical Magazine, v. 88, p. 61–89, https://doi.org/10.1180/mgm.2023.69.

Stalder, M., and Rozendaal, A., 2005, Trace and rare earth element chemistry of garnet and apatite as discriminant for Broken Hill-type mineralization, Namaqua Province, South Africa, *in* Mao, J., and Bierlein, F.P., eds., Mineral deposit research: Meeting the global challenge: Springer, p. 162–165, https://doi.org/10.1007/3-540-27946-6_178.

Suggate, S.M., and Hall, R., 2014, Using detrital garnet compositions to determine provenance: A new compositional database and procedure: Geological Society Special Publication, v. 386, p. 373–393, https://doi.org/10.1144/SP386.

Sverjensky, D.A., 1984, Europium redox equilibria in aqueous solution: Earth and Planetary Science Letters, v. 67, p. 70–78.

Swager, C.P., 1995, Geology of the greenstone terranes in the Kurnalpi-Edjudina region, southeastern Yilgarn craton: Western Australia Geological Survey Report, v. 47, p. 1–31.

Swager, C.P., 1997, Tectono-stratigraphy of the late Archaean greenstone terranes in the southern Eastern Goldfields, Western Australia: Precambrian Research, v. 83, p. 11–42, https://doi.org/10.1016/S0301-9268(97)00003-X.

Tappert, M., Rivard, B., Giles, D., Tappert, R., and Mauger, A., 2013, The mineral chemistry, near-infrared, and mid-infrared reflectance spectroscopy of phengite from the Olympic Dam IOCG deposit, South Australia: Ore Geology Reviews, v. 53, p. 26–38, https://doi.org/10.1016/j.oregeorev.2012.12.006.

Thompson, A., Scott, K.M., Huntington, J.F., and Yang, K., 2009, Mapping mineralogy with reflectance spectroscopy: Examples from volcanogenic massive sulfide deposits: Reviews in Economic Geology, v. 16, p. 25–40, https://doi.org/10.5382/Rev.16.04.

Tott, K.A., Spry, P.G., Pollock, M.V., Koenig, A., Both, R.A., and Ogierman, J., 2019, Ferromagnesian silicates and oxides as vectors to metamorphosed sediment-hosted Pb-Zn-Ag-(Cu-Au) deposits in the Cambrian Kanmantoo Group, South Australia: Journal of Geochemical Exploration, v. 200, p. 112–138, https://doi.org/10.1016/j.gexplo.2019.01.015.

Tual, L., Smit, M.A., Kooijman, E., Kielman-Schmitt, M., and Ratschbacher, L., 2022, Garnet, zircon, and monazite age and REE signatures in (ultra) high-temperature and high-pressure rocks: Examples from the Caledonides and the Pamir: Journal of Metamorphic Geology, v. 40, p. 1321–1346, https://doi.org/10.1111/jmg.12667.

van Ruitenbeek, F.J.A., Cudahy, T.J., van der Meer, F.D., and Hale, M., 2012, Characterization of the hydrothermal systems associated with Archean VMS-mineralization at Panorama, Western Australia, using hyperspectral, geochemical and geothermometric data: Ore Geology Reviews, v. 45, p. 33–46, https://doi.org/10.1016/j.oregeorev.2011.07.001.

van Westrenen, W., Allan, N.L., Blundy, J.D., Purton, J.A., and Wood, B.J., 2000, Atomistic simulation of trace element incorporation into garnets—comparison with experimental garnet-melt partitioning data: Geochimica et Cosmochimica Acta, v. 64, p. 1629–1639, https://doi.org/10.1016/S0016-7037(00)00336-7.

Walters, J.B., 2022, MinPlot: A mineral formula recalculation and plotting program for electron probe microanalysis: Mineralogia, v. 53, p. 51–66, https://doi.org/10.2478/mipo-2022-0005.

Wawryk, M., and Hancock, E.A., 2022, Portable XRF analysis in the Joe Lord and Perth Core Libraries—methodology and case studies: Geological Survey of Western Australia, Record 2022/11, 45 p.

Wiewiora, A., and Weiss, Z., 1990, Crystallochemical classifications of phyllosilicates based on the unified system of projection of chemical composition: II. The chlorite group: Clay Minerals, v. 25, p. 83–92, https://doi.org/10.1180/claymin.1990.025.1.09.

Wilkinson, J.J., Cooke, D.R., Baker, M.J., et al., 2017, Porphyry indicator minerals and their mineral chemistry as vectoring and fertility tools: Geological Survey of Canada, Open File 8345, p. 67–77, https://doi.org/10.4095/306305.

Williamson, B., Herrington, R.J., and Morris, A., 2016, Porphyry copper enrichment linked to excess aluminium in plagioclase: Nature Geoscience, v. 9, p. 237–241, https://doi.org/10.1038/ngeo2651.

Wilson, M.J., 2004, Weathering of the primary rock-forming minerals: Processes, products and rates: Clay Minerals, v. 39, p. 233–266, https://doi.org/10.1180/0009855043930133.

Witt, W., Cassidy, K., Lu, Y.J., and Hagemann, S., 2018, Syenitic Group intrusions of the Archean Kurnalpi terrane, Yilgarn craton: Hosts to ancient alkali porphyry gold deposits?: Ore Geology Reviews, v. 96, p. 262–268, https://doi.org/10.1016/j.oregeorev.2017.08.037.

Yang, K., Huntington, J.F., Gemmel, J.B., and Scott, K.M., 2011, Variations in composition and abundance of white mica in the hydrothermal alteration system at Hellyer, Tasmania, as revealed by infrared reflectance spectroscopy: Journal of Geochemical Exploration, v. 108, p. 143–156, https://doi.org/10.1016/j.gexplo.2011.01.001.

Yang, K.H., and Scott, S.D., 2006, Magmatic fluids as a source of metals in seafloor hydrothermal systems: American Geophysical Union, AGU Monograph, v. 166, p. 163–184.

Yardley, B.W.D., 1996, The evolution of fluids through the metamorphic cycle, *in* Jamtveit, B., and Yardley, B.W.D., eds., Fluid flow and transport in rocks: Chapman and Hall, p. 99–121.

Yardley, B.W.D., and Graham, J.T., 2002, The origins of salinity in metamorphic fluids: Geofluids, v. 2, p. 249–256, https://doi.org/10.1046/j.1468-8123.2002.00042.x.

Yardley, B.W.D., Rochelle, C.A., Barnicoat, A.C., and Lloyd, G.E., 1991, Oscillatory zoning in metamorphic minerals: An indicator of infiltration metasomatism: Mineralogical Magazine, v. 55, p. 357–365, https://doi.org/10.1180/minmag.1991.055.380.06.

Yeats, C.J., and Groves, D.I., 1998, The Archaean Mount Gibson gold deposits, Yilgarn craton, Western Australia: Products of combined synvolcanic and syntectonic alteration and mineralisation: Ore Geology Reviews, v. 113, p. 103–129, https://doi.org/10.1016/S0169-1368(97)00015-2.

Yeats, C.J., Hollis, S.P., Halfpenny, A., et al., 2017, Actively forming Kurokotype volcanic-hosted massive sulfide (VHMS) mineralization at Iheya North, Okinawa trough, Japan: Ore Geology Reviews, v. 84, p. 20–41, https://doi.org/10.1016/j.oregeorev.2016.12.014.

Yergeau, D., Mercier-Langevin, P., Dube, B., Malo, M., and Savoie, A., 2022, The Westwood deposit, southern Abitibi greenstone belt, Canada: An Archean Au-rich polymetallic magmatic-hydrothermal system—Part I. Volcanic architecture, deformation, and metamorphism: Economic Geology, v. 117, no. 3, p. 545–575, https://doi.org/10.5382/econgeo.4878.

Zane, A., and Weiss, Z., 1998, A procedure for classifying rock-forming chlorites based on microprobe data: Rendiconti Lincei, v. 9, p. 51–56, https://doi.org/10.1007/BF02904455.

Zang, W., and Fyfe, W., 1995, Chloritization of the hydrothermally altered bedrock at the Igarape-Bahia gold deposit, Carajas, Brazil: Mineralium Deposita, v. 30, p. 30–38, https://doi.org/10.1007/BF00208874.

Zhu, C., and Sverjensky, D.A., 1991, Partitioning of F-CI-OH between minerals and hydrothermal fluids: Geochimica et Cosmochimica Acta, v. 55, p. 1837–1858, https://doi.org/10.1016/0016-7037(91)90028-4.

Zivkovic, Z., Halley, S., Vicary, M., Baker, M., Cracknell, M.J., and Barker, S., 2024, Whole rock lithogeochemical analysis of the Mount Read Volcanics: A new tool for geochemical exploration: Geochemistry: Exploration, Environment, Analysis, v. 24, article geochem2024-008, https://doi.org/10.1144/geochem2024-008.

Cendi D.P. Dana is a final-year PhD candidate at the School of GeoSciences, the University of Edinburgh, where his research focuses on developing geochemical vectors to aid in the discovery of metamorphosed VMS deposits, particularly within Archean terranes. He holds an MSc in earth resource science from Akita University, Japan, and a bachelor's in geological engineering from Universitas Gadjah Mada, Indonesia. His current research integrates geochemistry, isotope analysis, and geochronology to investigate ore-forming processes in magmatic-hydrothermal systems (e.g., porphyry, skarn, epithermal, and VMS) and their implications for mineral exploration. In addition to his academic work, he has industry experiences in both greenfield and brownfield exploration, particularly for epithermal and skarn deposits.